Ocean Sci. Discuss., 8, 2417–2478, 2011
www.ocean-sci-discuss.net/8/2417/2011/
doi:10.5194/osd-8-2417-2011

Ocean Science Discussions

Three-dimensional modelling of wave-induced current from the surf zone to the inner shelf

H. Michaud[1,2], P. Marsaleix[2], Y. Leredde[1], C. Estournel[2], F. Bourrin[3], F. Lyard[4], C. Mayet[4], and F. Ardhuin[5]

[1]Géosciences Montpellier, UMR5243, CNRS – Université Montpellier 2 Sciences et Techniques, place E Bataillon, 34095 Montpellier cedex 5, France
[2]Laboratoire d'Aérologie, UMR5560, CNRS – Université de Toulouse, 14 avenue Edouard Belin, 31400 Toulouse, France
[3]Centre de Formation et de Recherche sur l'Environnement Marin, UMR5110, CNRS – Univ. de Perpignan Via Domitia, 52 avenue de Villeneuve, 66860 Perpignan cedex, France
[4]Laboratoire d'Etudes en Géophysique et Océanographie Spatiales (CNRS/CNES/IRD/UPS), 14 avenue Edouard Belin, 31400 Toulouse, France
[5]IFREMER, Centre de Brest, Laboratoire d'Océanographie Spatiale, 29280 Plouzané, France

Received: 13 October 2011 – Accepted: 25 November 2011 – Published: 9 December 2011

Correspondence to: H. Michaud (michaud.heloise@aero.obs-mip.fr)

Published by Copernicus Publications on behalf of the European Geosciences Union.

Abstract

We develop and implement a new method to take into account the impact of waves into the 3-D circulation model SYMPHONIE (Marsaleix et al., 2008, 2009a), following the simplified equations of Bennis et al. (2011) which use glm2z-RANS theory (Ardhuin et al., 2008b). These adiabatic equations are completed by additional parameterizations of wave breaking, bottom friction and wave-enhanced vertical mixing, making the forcing valid from the surf zone through to the open ocean. The wave forcing is performed by wave generation and propagation models WAVEWATCH III® (Tolman, 2008, 2009; Ardhuin et al., 2010) and SWAN (Booij et al., 1999). The model is tested and compared with other models for a plane beach test case, previously tested by Haas and Warner (2009) and Uchiyama et al. (2010). A comparison is also made with the laboratory measurements of Haller et al. (2002) of a barred beach with channels. Results fit with previous simulations performed by other models and with available observational data.

Finally, a realistic case of energetic waves travelling over a coast of the Gulf of Lion (in the northwest of the Mediterranean Sea) for which currents are available at different depths as well as an accurate bathymetric database of the 0–10 m depth range, is then simulated. A grid nesting approach is used to account for the different forcings acting at different spatial scales. The simulation coupling the effects of waves and currents is successful to reproduce the powerful northward littoral drift in the 0–15 m depth zone. More precisely, two distinct cases are identified: when waves have a normal angle of incidence with the coast, they are responsible for complex circulation cells and rip currents in the surf zone, and when they travel obliquely, they generate a northward littoral drift. These features are more complicated than in the test cases, due to the complex bathymetry and the consideration of wind and non-stationary processes. Wave impacts in the inner shelf are less visible since wind and regional circulation seem to be the predominant forcings. Besides, a discrepancy between model and observations is noted at that scale, possibly linked to an underestimation of the wind

OSD

8, 2417–2478, 2011

stress. Lastly, this three-dimensional method allows a good representation of vertical current profiles and permits to calculate the shear stress associated with wave and current. Future work will focus on the combination with a sediment transport model.

1 Introduction

Over the past half-century, considerable advances have been made in the field of numerical modelling of coastal hydrodynamics, with major efforts made to take wave-current interactions into account. Such studies have allowed the investigation of beach protection, contaminant monitoring, navigational issues, coastal management and prediction of hazardous zones for swimmers. A wide variety of modelling techniques have been applied to the surf zone, based on depth-integrated equations. These include phase resolving (e.g. Chen et al., 2003; Clark et al., 2011), group-averaged Reniers et al. (2004), or fully phase-averaged. These models are unfortunately not well adapted for continental shelf processes that are influenced by stratification, making it difficult to model cross-shore transport phenomena uniformly from the beach to the shelf break. Recently developed 3-D wave-current interaction theories (e.g. Mellor, 2003; McWilliams et al., 2004; Ardhuin et al., 2008b) may provide useful approaches for this problem.

Following the pioneering modeling work by Rascle (2007); Newberger and Allen (2007); Uchiyama et al. (2010), we investigate the influence of surface waves on ocean circulation in the inner shelf and surf zone. The main influences of waves on current occur through bottom (e.g. Komar et al., 1972) and surface stresses (e.g. Donelan et al., 1993), while turbulent kinetic energy at the surface is enhanced by wave breaking (e.g. Agrawal et al., 1992). Waves are associated with mean momentum that can be observed as a surface-intensified drift velocity (Stokes, 1847). In deep water, this drift is highly correlated with the wind speed and wave height, with a magnitude of the order $6 \times 10^{-4} U_{10}^2$ where U_{10}, the 10 m wind speed, is in $\mathrm{m\,s^{-1}}$ (Ardhuin et al., 2009). In the surf zone, the drift is not correlated with wind speed and can reach as much as 30 % of

OSD
8, 2417–2478, 2011

the phase speed, with a strong surface intensification (Ardhuin et al., 2008b). The actual drift of water particles is the sum of this Stokes drift and the Eulerian current, with wave influences on the Eulerian current also (e.g. Xu and Bowen, 1994). Reciprocally, currents can modify waves by, refraction, partial reflection, up to blocking (Smith, 1975; Chawla and Kirby, 2002).

A first approach to the study of wave/current interactions can be to add certain effects in particular contexts (e.g. Jorda et al., 2007). For example, Mastenbroek et al. (1993) improve their numerical simulations of storm surges by introducing a wave-dependent drag coefficient for the wind.

During the 1960's, Taylor (1962) and Whitham (1962) focused on non-linear wave properties. These works then led to the radiation stress theory, which was first introduced by Longuet-Higgins and Stewart (1962), and then by Phillips (1977). This theory takes into account the excess flow of momentum due to the presence of waves in the barotropic momentum equations for the total current, thanks to the addition of radiation stress gradients. In radiation stress theory, wave and current momenta are combined and the effect of the waves is applied to this total momentum. Although this is practical for depth-integrated flows, it becomes a problem in 3-D models, in particular because the Stokes drift is not mixed and is often the main source of vertical shear near the surface, with important consequences for surface drift (e.g. Rascle and Ardhuin, 2009). Instead, the problem can be formulated for the current momentum only, as shown by Garrett (1976) for depth-integrated equations, and Andrews and McIntyre (1978) in the most general form. Several theories have been developed and applied for the full momentum (involving radiation stresses) or the current momentum only (in which a vortex force appears). Although much work is still to be developed for the proper treatment of turbulence in the presence of waves, several papers have established that all published theories that use radiation stresses have some errors at the leading order, which may cause spurious circulations (Ardhuin et al., 2008a; Kumar et al., 2011; Bennis and Ardhuin, 2011).

OSD
8, 2417–2478, 2011

Here we shall use a formulation of the "current momentum" which is formally defined as the quasi-Eulerian momentum (Andrews and McIntyre, 1978; Jenkins, 1989), namely the Lagrangian mean velocity minus the Stokes drift. Here we use an approximation of the exact equations from (Andrews and McIntyre, 1978) to second order in wave slope, including a transformation to cartesian coordinates (glm2-z approximation, Ardhuin et al., 2008b), in a simplified form that neglects the vertical current shear effect on the dynamic pressure (Bennis et al., 2011). In the limit of weak vertical current shear, these equations are formally equivalent to the Eulerian-mean equations of McWilliams et al. (2004) that are based on an analytic continuation across the air-sea interface, and which have been used by Uchiyama et al. (2010).

Previous studies dealing with wave-current interaction are often focused on the surf zone (with water depths on the order of 1 m) (e.g. Uchiyama et al., 2010; Haas and Warner, 2009; Weir et al., 2011). Few studies and measurements have been dedicated to the midshelf zone (with water depths of order 100 m), or at least to the inner shelf (between the surf zone and mid shelf): Lentz et al. (1999, 2008) were one of the first to study the influence of waves on the inner shelf. The purpose of this article is to extend the study of wave-current interaction to both the inner shelf and the open ocean by implementing the new set of equations of Bennis et al. (2011) in the primitive equation model SYMPHONIE (Marsaleix et al., 2008). By using a nested strategy, which allows studies at all scales and by completing the model with additional parameterizations of wave breaking, bottom friction and wave-enhanced vertical mixing, we ensure that the forcing is valid from the surf zone through to the open ocean. We test and compare our model to measurements made on the Têt inner shelf during a typical winter storm. This inner shelf has a bathymetry made up of complex sandbar systems, therefore before tackling this real case, the accuracy of the model is first assessed in two idealized test cases.

Wave and circulation models, modified with the formulation of Bennis et al. (2011), are presented in Sect. 2. Section 3 describes two academic test cases of the surf zone. The first is on an idealized plane beach submitted to obliquely incident spectral

OSD
8, 2417–2478, 2011

waves (a case also tested by Haas and Warner, 2009 and Uchiyama et al., 2010). The second case tests the ability of the model to correctly reproduce rip currents generated by a barred beach, by simulating the test B experiment of Haller et al., 2002). Section 4 focuses on the 21 February 2004 storm in the Têt inner shelf. The simulated currents are compared to the observed ones to assess model accuracy. Finally, Sect. 5 provides a summary and conclusion.

2 Models

2.1 Coastal Circulation Model

We used the Boussinesq hydrostatic circulation ocean model described in Marsaleix et al. (2008, 2009a,b). Components of currents, temperature and salinity are computed on a C-grid using an energy-conserving finite-difference method. A generalized sigma coordinate (Ulses et al., 2008c) is used in order to refine resolution near the bottom and the surface. The turbulence closure is achieved using a prognostic equation for the turbulence kinetic energy and a diagnostic equation for mixing and dissipation length scales proposed by Bougeault and Lacarrere (1989). A complete description of the bulk formulae used to compute the air/sea fluxes is given in Estournel et al. (2009). The so called SYMPHONIE model has been extensively used in studies of the Mediterranean Sea, mostly at the scale of continental shelves (Ulses, 2005; Estournel et al., 2003; Estournel et al., 2005), generally comparing satisfactorily with available in situ observations. Only Leredde and Michaud (2008) found that the model did not perform that well for the case of an extreme meteorological event reported in the Gulf of Lion in February 2007. It was concluded that the relative failure of the simulations was likely a consequence of the lack of a proper wave/current parameterization. This study incited the present one, in which we implement this particular development in our model, following the method proposed by Bennis et al. (2011).

OSD
8, 2417–2478, 2011

2.1.1 General equations

The momentum equations of the coastal circulation model are rewritten in order to take into account the wave forcing. This gives the Eqs. (18)–(21) of Bennis et al. (2011) which govern the evolution of the quasi-Eulerian velocities $(\hat{u},\hat{v},\hat{w})$ equal to:

$$(\hat{u},\hat{v},\hat{w}) = (u,v,w) - (U_s,V_s,W_s) \quad (1)$$

where (u,v,w) are the mean Lagrangian velocities and (U_s,V_s,W_s) the Stokes drift in the horizontal (x,y) and vertical (z) directions. They are valid from the bottom $z=-h$ to the local phase-averaged free surface $z=\hat{\eta}$.

$$\frac{\partial \hat{u}}{\partial t}+\hat{u}\frac{\partial \hat{u}}{\partial x}+\hat{v}\frac{\partial \hat{u}}{\partial y}+\hat{w}\frac{\partial \hat{u}}{\partial z}-f\hat{v}+\frac{1}{\rho}\frac{\partial p^{H}}{\partial x}=\left[f+\left(\frac{\partial \hat{v}}{\partial x}-\frac{\partial \hat{u}}{\partial y}\right)\right]V_s-W_s\frac{\partial \hat{u}}{\partial z}-\frac{\partial J}{\partial x}+F_{m,x}+F_{d,x} \quad (2)$$

$$\frac{\partial \hat{v}}{\partial t}+\hat{u}\frac{\partial \hat{v}}{\partial x}+\hat{v}\frac{\partial \hat{v}}{\partial y}+\hat{w}\frac{\partial \hat{v}}{\partial z}+f\hat{u}+\frac{1}{\rho}\frac{\partial p^{H}}{\partial y}=-\left[f+\left(\frac{\partial \hat{v}}{\partial x}-\frac{\partial \hat{u}}{\partial y}\right)\right]U_s-W_s\frac{\partial \hat{v}}{\partial z}-\frac{\partial J}{\partial y}+F_{m,y}+F_{d,y} \quad (3)$$

With p^H the hydrostatic pressure, f the Coriolis parameter, ρ the mean density and t the time. The forces added by the wave forcing in the momentum equation are:

- the vortex force: $([\frac{\partial \hat{v}}{\partial x}-\frac{\partial \hat{u}}{\partial y}]V_s-W_s\frac{\partial \hat{u}}{\partial z},[\frac{\partial \hat{v}}{\partial x}-\frac{\partial \hat{u}}{\partial y}]U_s-W_s\frac{\partial \hat{v}}{\partial z})$
- the Stokes-Coriolis force: $(fV_s,-fU_s)$
- the force linked to the wave-induced mean pressure J called the Bernouilli pressure head: $(-\frac{\partial J}{\partial x},-\frac{\partial J}{\partial y})$
- the mixing force where some parameterizations of the wave-enhanced mixing are taken into account: $(F_{m,x},F_{m,y})$
- the force of dissipation by breaking, bottom dissipation and wave-turbulence interaction: $(F_{d,x},F_{d,y})$

OSD
8, 2417–2478, 2011

The evolution of C the concentration of a passive tracer is then governed by:

$$\frac{\partial C}{\partial t} + \frac{\partial uC}{\partial x} + \frac{\partial vC}{\partial y} + \frac{\partial wC}{\partial z} = 0 \tag{4}$$

And the mass conservation becomes:

$$\frac{\partial u}{\partial x} + \frac{\partial v}{\partial y} + \frac{\partial w}{\partial z} = 0 \tag{5}$$

These equations were implemented in the MARS 3-D model (Lazure and Dumas, 2008). We transform them into a discrete form by using the flux-divergence form of the advection terms which can be found in most coastal hydrodynamic models (e.g. Marsaleix et al., 2008; Blumberg and Mellor, 1987; Shchepetkin and McWilliams, 2005). They then become:

$$\frac{\partial \hat{u}}{\partial t} + \frac{\partial u\hat{u}}{\partial x} + \frac{\partial v\hat{u}}{\partial y} + \frac{\partial w\hat{u}}{\partial z} - f\hat{v} + \frac{1}{\rho}\frac{\partial p^{\mathrm{H}}}{\partial x} = fV_{\mathrm{s}} + \frac{\partial \hat{u}}{\partial x}U_{\mathrm{s}} + \frac{\partial \hat{v}}{\partial x}V_{\mathrm{s}} - \frac{\partial J}{\partial x} + F_{\mathrm{m},x} + F_{\mathrm{d},x} \tag{6}$$

$$\frac{\partial \hat{v}}{\partial t} + \frac{\partial u\hat{v}}{\partial x} + \frac{\partial v\hat{v}}{\partial y} + \frac{\partial w\hat{v}}{\partial z} + f\hat{u} + \frac{1}{\rho}\frac{\partial p^{\mathrm{H}}}{\partial y} = -fU_{\mathrm{s}} + \frac{\partial \hat{u}}{\partial y}U_{\mathrm{s}} + \frac{\partial \hat{v}}{\partial y}V_{\mathrm{s}} - \frac{\partial J}{\partial y} + F_{\mathrm{m},y} + F_{\mathrm{d},y} \tag{7}$$

This choice allows a global calculation of the term $w = \hat{w} + W_{\mathrm{s}}$ and the calculation of the value W_{s} is no longer needed. In the new set of equations, the vortex force does not appear clearly and is replaced by a new force equal to $(\frac{\partial \hat{u}}{\partial x}U_{\mathrm{s}} + \frac{\partial \hat{v}}{\partial x}V_{\mathrm{s}}\ ,\ \frac{\partial \hat{u}}{\partial y}U_{\mathrm{s}} + \frac{\partial \hat{v}}{\partial y}V_{\mathrm{s}})$. But we note that we can get back to the usual vortex force provided that the Stokes current contribution to the advection terms, namely, $(\frac{\partial U_{\mathrm{s}}\hat{u}}{\partial x} + \frac{\partial V_{\mathrm{s}}\hat{u}}{\partial y} + \frac{\partial W_{\mathrm{s}}\hat{u}}{\partial z}, \frac{\partial U_{\mathrm{s}}\hat{v}}{\partial x} + \frac{\partial V_{\mathrm{s}}\hat{v}}{\partial y} + \frac{\partial W_{\mathrm{s}}\hat{v}}{\partial z})$, is taken into account.

Calculations of wave-induced pressure J are not modified from Bennis et al. (2011):

$$J = g\frac{kE}{\sinh(2kD)} \tag{8}$$

OSD
8, 2417–2478, 2011

Stokes velocities are given by:

$$\begin{cases} (U_s, V_s) = \sigma k(\cos\theta, \sin\theta) E \frac{2\cdot\cosh(2k(z+h))}{\cosh(2kD)} \\ \text{in shallow waters for } \; kD < 6 \\ \text{and } \; (U_s, V_s) = \sigma k(\cos\theta, \sin\theta) E 2e^{2\cdot k(z-\eta)} \\ \text{in deep waters for } kD > 6 \end{cases} \tag{9}$$

with $D = \eta + h$ the water depth, g the acceleration due to gravity, E the wave energy, k the wave number, σ the relative frequency and θ the angle of wave propagation.

In realistic configurations (i.e. for random waves), we replace E by the elementary variance $E(\theta, \sigma) d\theta d\sigma$ and we integrate the entire expression over the spectrum of the relative frequencies and angles of wave propagation of the wave model. The WAVEWATCH III wave model, hereinafter WW3 (version 4.04-SHOM; Tolman, 2008, 2009; Ardhuin et al., 2010), provides directly the wave-induced pressure. It also gives the surface Stokes velocities ($(U_{sf}(k_n), V_{sf}(k_n) = w_n k_n E$) discretized in the frequency spectrum, so the Stokes drift can be calculated by summing these terms over the frequency spectrum:

$$(U_s, V_s) = \sum_{k_n} (U_{sf}(k_n), V_{sf}(k_n)) P(z; k_n) \tag{10}$$

with k_n the wave numbers associated to the different frequencies of the spectrum. w_n are calculated by $w_n = \sqrt{g k_n \tanh(k_n D)}$ and $P(z; k_n)$, the vertical profiles associated with the different frequencies, are defined by:

$$\begin{cases} P(z; k_n) = \frac{2\cdot\cosh(2k_n(z+h))}{\cosh(2k_n D)} \text{ in shallow waters for } k_n D < 6 \\ P(z; k_n) = 2e^{2\cdot k_n(z-\eta)} \text{ in deep waters for } \; k_n D > 6. \end{cases} \tag{11}$$

Stokes drift is strongly sheared at the surface so a high resolution near the surface is required.

OSD
8, 2417–2478, 2011

In these equations, the wave-induced dissipation force as defined by Bennis et al. (2011) is split into two forces: one associated with wave-breaking dissipation (bathymetric breaking and whitecapping), and one induced by bottom dissipation. In the absence of a known vertical profile, these two forces find themselves in the boundary conditions respectively at the surface and at the bottom as surface and bottom stresses. One can thus impose an empirical vertical profile for the two forces (Bennis et al., 2011; Uchiyama et al., 2010). On the other hand, the vertical profile of velocity is possibly not really sensitive to such issues because of the smoothing effects induced by strong vertical mixing (Rascle et al., 2006).

2.1.2 Boundary conditions

Boundary conditions then become:

– At the surface:

$$\begin{cases} K_z \frac{\partial \hat{u}}{\partial z}|_{z=\hat{\eta}} = \tau_{a,x} - \tau_{aw,x} + \tau_{wo,x} \\ K_z \frac{\partial \hat{v}}{\partial z}|_{z=\hat{\eta}} = \tau_{a,y} - \tau_{aw,y} + \tau_{wo,y} \end{cases} \quad (12)$$

with K_z the vertical eddy viscosity calculated by a turbulent closure scheme representing the energy cascade towards small scales (Gaspar et al., 1990). $\boldsymbol{\tau}_a = (\tau_{a,x}, \tau_{a,y})$ the wind stress, $\boldsymbol{\tau}_{aw} = (\tau_{aw,x}, \tau_{aw,y})$ the momentum flux from atmosphere to wave, and $\boldsymbol{\tau}_{wo} = (\tau_{wo,x}, \tau_{wo,y})$ the momentum flux from wave to ocean linked to wave breaking (bathymetric breaking, or whitecapping), wave-turbulence interaction and viscous effects. In fact, waves influence the flux transfers from atmosphere to ocean. A part of the atmosphere momentum flux goes directly in the ocean via $\boldsymbol{\tau}_a$. Another part $\boldsymbol{\tau}_{aw}$ goes into the wave field. Then this field is subjected to dissipation and releases $\boldsymbol{\tau}_{wo}$. At a larger scale than the surf zone, $\boldsymbol{\tau}_{aw}$ and $\boldsymbol{\tau}_{wo}$ tend to cancel each other. Actually, only a small part of $\boldsymbol{\tau}_{aw}$ (5 %) is radiated into the wave field (Ardhuin et al., 2004). WW3 provides directly these terms. In the surf zone, the term $\boldsymbol{\tau}_{wo}$ is predominant, and $\boldsymbol{\tau}_{aw}$ is neglected. For monochromatic waves, we link $\boldsymbol{\tau}_{wo}$ to the wave dissipation due to wave breaking ϵ^b used by Uchiyama et al. (2010), by:

OSD
8, 2417–2478, 2011

$$\boldsymbol{\tau}_{\mathrm{wo}} = \frac{\epsilon^{\mathrm{b}} \boldsymbol{k}}{\sigma} \tag{13}$$

In fact, this ratio is often used in the literature, and given as a $\frac{1}{\rho g}$ factor by the Simulating Waves Nearshore wave model (SWAN-version 40.72 ; Booij et al., 1999).

– On the bottom:
We consider that the momentum lost by waves due to bottom friction is lost in the bottom (Longuet-Higgins, 2005), and we follow the Eq. (22) of Bennis et al. (2011) which sets that the horizontal velocity is prescribed as velocity at the bottom given by the streaming solution (Longuet-Higgins, 1953):

$$(\hat{u}, \hat{v})|_{z=-h} = 1.5(U_{\mathrm{s}}, V_{\mathrm{s}})|_{z=-h} \tag{14}$$

– Lateral boundaries:
At the open boundaries, for realistic simulations, radiation conditions from Flather (1976) are applied. Technically, we follow the Eq. (14) of Marsaleix et al. (2006). Thus, for the sea surface elevation external variable:

$$\eta = \eta_{\mathrm{F}} \pm \sqrt{\frac{D}{g}(\hat{u}^{\mathrm{N}} - u_{\mathrm{F}}^{\mathrm{N}})} \tag{15}$$

where $\hat{u}^{\mathrm{N}}$ is the velocity normal to the boundary, and "F" refers to the external forcing term. If waves are the only external forcing:

$$\begin{cases} \eta_{\mathrm{F}} = -\frac{J}{g} \\ \hat{u_{\mathrm{F}}}^{\mathrm{N}} = -U_{\mathrm{s}}^{\mathrm{N}}. \end{cases} \tag{16}$$

Boundary conditions (Eq. 16) are deduced from the momentum equation (Eqs. 2 and 3) and some simplifying hypotheses (steady solution, non linear terms are neglected).

OSD
8, 2417–2478, 2011

2.1.3 Wave-induced vertical mixing

Vertical mixing is parameterized according to the turbulent closure model of Gaspar et al. (1990). The vertical eddy viscosity K_z is calculated by: $K_z = c_k l_k E_k^{0.5}$ with E_k the turbulent kinetic energy, $c_k = 0.1$ an empirical constant and l_k an algebraic length. The turbulent kinetic energy is characterized by:

$$\frac{\partial E_k}{\partial t} + \frac{\partial \hat{u} E_k}{\partial x} + \frac{\partial \hat{v} E_k}{\partial y} + \frac{\partial \hat{w} E_k}{\partial z} = K_z \left[(\frac{\partial \hat{u}}{\partial z})^2 + (\frac{\partial \hat{v}}{\partial z})^2 \right] + \frac{g}{\rho_0} K_z \frac{\partial \rho}{\partial x} + \frac{\partial}{\partial z}(F_z) - \frac{c_\epsilon E_k^{3/2}}{l_\epsilon} \quad (17)$$

c_ϵ is also an empirical constant equal to 0.7, and l_ϵ is the dissipation length. l_k and l_ϵ are calculated according to Bougeault and Lacarrere (1989). F_z is a vertical flux of turbulent kinetic energy equal to $K_z \frac{\partial E_k}{\partial z}$.

The wave forcing modifies the eddy diffusivity both at the surface and at the bottom.

– At the surface:
Waves modify the turbulent mixing in the surface layer by adding certain quantities in the turbulent closure models. We follow Craig and Banner (1994) by taking into account the dissipation of surface waves by adding a turbulent kinetic energy flux at the surface. Thus, F_z is modified:

$$\begin{cases} F_z = \phi_{oc} & \text{near the surface} \\ F_z = K_z \frac{\partial E_k}{\partial z} & \text{elsewhere} \end{cases} \quad (18)$$

A possible parameterization of the wave to ocean turbulent surface flux is (Terray et al., 1996):

$$\phi_{oc} = \alpha u_\star^3 \quad (19)$$

where $u_\star$, the friction velocity, is deduced from the wind stress, and α is a parameter linked to the wave age. By default, this term is equal to 100 (Craig and Banner, 1994).

OSD
8, 2417–2478, 2011

Estournel et al. (2001) showed that the depth of the surface mixed layer was better simulated with the Craig and Banner scheme rather than with a boundary condition based on an assumption of production/dissipation equilibrium in the turbulent kinetic energy equation. On the other hand, following Rascle et al. (2008), we used an alternative that is, a priori, more accurate: to use the wave to ocean turbulent surface flux provided by the WW3 model. The mixing length is also modified:

$$l = \kappa z_{\text{surf}} \tag{20}$$

where $\kappa = 0.4$ is the Von Karman constant and z_{surf} is the surface roughness length. It corresponds to the depth of the wave breaking responsible for the increase of turbulent mixing. Terray et al. (1996, 2000) used dissipation data to link this term to the significant wave height: $z_{\text{surf}} = 1.6\,H_{\text{s}}$. We therefore tested values between $0.8\,H_{\text{s}}$ and $2.4\,H_{\text{s}}$ which can be found in the literature (Rascle et al., 2006). Ideally, we should not use the significant wave height, but the significant wave height of the wind-sea only H_{sw}. Given that the swells have a small surface slope and consequently do not break, it is more appropriate to use the wave height of the wind sea only to calculate the roughness length instead of the significant wave height H_{s} (Rascle et al., 2008). This value is calculated according to Rascle et al. (2008) (Eq. 6), and is now available in WW3.

– On the bottom:

In our hydrodynamic model, the bottom stress ($\boldsymbol{\tau}_{\text{bot}}$ in Eq. (14) is parameterized by a quadratic bottom drag model and is only linked to the current through:

$$\boldsymbol{\tau}_{\text{bot}} = \boldsymbol{\tau}_{\text{c}} = \rho_0 C_{\text{d}} \| \boldsymbol{V}_{\text{b}} \| \boldsymbol{V}_{\text{b}} \tag{21}$$

with C_{d} the drag coefficient and $\boldsymbol{V}_{\text{b}}$ the near bottom current.

Waves enhance the shear stress at the bottom. Soulsby et al. (1995) have established a drag law function of the bottom stresses linked to waves and currents:

$$\boldsymbol{\tau}_{\text{bot}} = \boldsymbol{\tau}_{\text{c}}\left[1 + 1.2\left(\frac{|\tau_{\text{w}}|}{|\tau_{\text{w}}| + |\boldsymbol{\tau}_{\text{c}}|}\right)^{3.2}\right] \tag{22}$$

OSD
8, 2417–2478, 2011

with $\boldsymbol{\tau}_c$ the bottom stress due to current only, calculated by Eq. (21) and τ_w the bottom stress linked to waves only, given by:

$$|\tau_w| = 0.5 f_w |\boldsymbol{u}_{orb}|^2. \quad (23)$$

$\boldsymbol{u}_{orb}$ is the bottom wave orbital velocity, calculated, for monochromatic waves, by:

$$|\boldsymbol{u}_{orb}| = \frac{\sigma H_s}{\sqrt{8 \sinh(kD)}} \quad (24)$$

For random waves, we integrate the expression of $\boldsymbol{u}_{orb}$ over the spectrum of the relative frequencies and angles of wave propagation of the wave model. WW3 provides directly this term. f_w the wave friction factor given by Myrhaug et al. (2001):

$$\begin{cases} f_w = 1.39 \left(\frac{a_{bw}}{z_0}\right)^{-0.52} & \text{if} \quad 200 < \frac{a_{bw}}{z_0} < 11\,000 \\ f_w = 18 \left(\frac{a_{bw}}{z_0}\right)^{-1} & \text{if} \quad \frac{a_{bw}}{z_0} < 200 \\ f_w = 0.112 \left(\frac{a_{bw}}{z_0}\right)^{-0.25} & \text{if} \quad 11\,000 < \frac{a_{bw}}{z_0} \end{cases} \quad (25)$$

with z_0 the bottom roughness length and a_{bw} the half orbital excursion length is given by $a_{bw} = \frac{|u_{orb}|T}{2\pi}$ (with T the wave period). With this parameterization, the bottom stress is increased since it lies in the range: $\tau_c < \tau_{bot} < 2.2\tau_c$. In the two test cases, we use the bottom stress parameterized by Eq. (21), and in the realistic simulation we use the parameterization of Eq. (22).

2.2 Wave model

In order to take into account the effects of waves in the momentum equations, some quantities provided by wave models are required: period, significant wave height, direction, wavenumber, Stokes velocities, wavelength, $\boldsymbol{\tau}_{aw}$ the momentum flux from atmosphere to wave, and $\boldsymbol{\tau}_{wo}$ the momentum flux from wave to ocean linked to wave breaking. Some of them can be directly provided by the wave model, and others can be calculated from the available parameters, depending on the wave model chosen.

OSD
8, 2417–2478, 2011

In the academic case studies, presented in Sect. 3, we use the SWAN wave model, and in the realistic simulation, presented in Sect. 4, we use the WW3 model, validated at global, regional and nearshore scales. These are third generation wave-averaged models that solve the two dimensional wave action balance equations for wave action density as a function of (θ,σ) for the SWAN model and a function of (θ,k) for the WW3 model. In Cartesian coordinates, this equation is written as:

$$\frac{\partial N}{\partial t}+\frac{\partial c_x N}{\partial x}+\frac{\partial c_y N}{\partial y}+\frac{\partial c_\sigma N}{\partial \sigma}+\frac{\partial c_\theta N}{\partial \theta}=\frac{S_{\text{tot}}}{\sigma} \tag{26}$$

with N the wave action density $N=\frac{E}{\sigma}$, c_x, c_y, c_σ and c_θ the propagation velocities in x-, y-, σ- and θ-space, respectively. The source/sink term, S_{tot} on the right side, is expressed in terms of energy density and represents different physical processes available in the wave model:

$$S_{\text{tot}}=S_{\text{in}}+S_{\text{nl3}}+S_{\text{nl4}}+S_{\text{ds,w}}+S_{\text{ds,b}}+S_{\text{ds,br}} \tag{27}$$

with S_{in} the atmospheric source function, S_{nl4} the nonlinear quadruplet interactions and $S_{\text{ds,w}}$ the dissipation by whitecapping. Other phenomena induced by the finite depth effects like S_{nl3} triad nonlinear wave-wave interactions, $S_{\text{ds,b}}$ dissipation by bottom friction and $S_{\text{Sds,br}}$ dissipation by depth-induced breaking are taken into account. Thus, diffraction, reflection, refraction and shoaling are included.

SWAN (version 40.72) accounts for all these processes. It is generally used for wave transformation at nearshore and coastal scales (Booij et al., 1999; Dufois, 2008; Rusu and Soares, 2009; Bruneau, 2009). We will use this model for the academic cases.

WW3 has been widely used at global and regional scales and its validity is now extended to nearshore scales (version 4.04) with parameterizations of wave breaking, bottom dissipation and wave dissipation, avoiding the use of a specific nearshore wave model. One can find more information about the parameterizations proposed by this version in Ardhuin et al. (2010). This model has been validated using in-situ and remote sensing data (Ardhuin et al., 2008c, 2010; Delpey et al., 2010).

OSD
8, 2417–2478, 2011

3 Validation of the model in two test cases

3.1 A normal plane beach test case

This test case consists of obliquely incident spectral waves approaching an idealized smooth plane beach. It was initially posed by Haas and Warner (2009), hereinafter named HW09 and more recently by Uchiyama et al. (2010), hereinafter called UMS10. HW09 compared two hydrodynamic models: the quasi-3-D model SHORECIRC (Svendsen et al., 2002) and the 3-D model ROMS (Shchepetkin and McWilliams, 2005), where wave forcing followed the depth-dependent radiation stress formalism of Mellor (2003). UMS10 compared these solutions with another version of ROMS where a vortex force (McWilliams et al., 2004) approach is used. All these solutions were forced rigorously by the same wave field simulated by SWAN. We suggest comparing our model to this test case to assess its validity and performance to those of previous models.

The bathymetry is a plane beach with a constant slope of 1:80. It has realistic dimensions (1180 m in the cross-shore direction x and 1200 m in the alongshore direction y). The coast is oriented to the west and the offshore boundary is set at $x = 0$ with the maximum water depth (12 m). We use the same grid spacing of 20 m in horizontal directions as in previous simulations, and 10 vertical levels. To be consistent with UMS10 and HW09, a quadratic bottom drag law (Eq. 21) is used with a drag coefficient C_d sets constant equal to 0.0015.

At the offshore boundary, a Jonswap type spectral modeled wave field is imposed with a 2 m significant wave height, 10 s peak period and an incidence angle of 10°. We use the same wave fields as HW09 and UMS10. We also neglect the roller effects. Earth rotation is excluded with the Coriolis parameter set to 0. Lateral periodic conditions are used. As a first step, we do not take into account the influence of waves on vertical mixing and on the surface roughness length. UMS10 conducted four simulations: a 2-D barotropic case (Run a) and three 3-D cases where the vertical profiles of the vector of breaking dissipation or the vertical mixing are changed (Runs b, c and d).

OSD
8, 2417–2478, 2011

In Run b, the vertical penetration of momentum associated with breaking waves is concentrated near the surface, whereas in Runs c and d, penetration is quite uniform along the vertical column. Run b gives results similar to ours, since our model adds the momentum associated with breaking waves as a surface stress. UMS10 also calculated an analytical solution for the barotropic velocities and the surface elevation.

3.1.1 Reference simulation

Waves begin to break between $500 < x < 1000$ m, (as shown by the breaking dissipation rate Fig. 16a. in UMS10), and the significant wave height decreases for $x = 600$ m. A slight set-down before the breaking point and a set-up reaching 22 cm at the shoreline are observed. After two hours of simulation time, our simulation becomes stationary. Our surface elevation agrees well with both the analytical and numerical results of UMS10 (Fig. 1a). The cross-shore barotropic velocity (Fig. 1b) is the same as that of UMS10 and the alongshore barotropic velocity (Fig. 1c) almost fits the results from Run b, with a maximum value of $0.85\,\mathrm{m\,s^{-1}}$ located closer onshore ($x = 820$ m) than other runs. Our peak alongshore barotropic velocity underestimates the peak value obtained in Run b of UMS10. As we will see in Sect. 4.1.2, this is explained by the fact that in our case, the momentum flux associated with breaking waves is prescribed as a surface stress, whereas in the work of UMS10 the momentum flux has a vertical profile (concentrated near the surface). Vertical profiles of the velocities (Fig. 2) are also consistent with the vertical profiles of Run b. Note the color palette is not saturated as in UMS10, in order to show how the cross-shore velocities are sheared ($0.6\,\mathrm{m\,s^{-1}}$ near the surface to $-0.6\,\mathrm{m\,s^{-1}}$ close to the bottom). We therefore obtain a strong and common recirculation cell in the surf zone with the current oriented onshore near the surface and offshore on the bottom. Outside of the surf zone, cross-shore velocities are almost uniform over the depth and directed offshore. They are the exact opposite of the Stokes velocities. Here we consider only a test case thus no other external forcing, such as wind stress, is taken into account. It is therefore not necessary to represent all the terms of the momentum equations, but only the ones linked to the wave forcing.

OSD
8, 2417–2478, 2011

The wave forcing acts directly on the mean flow by way of the following forces:

- The vortex force.
- The Bernouilli pressure head.
- The surface flux of momentum associated with breaking wave dissipation (bathymetric breaking and whitecapping).

We describe in detail how these forces are balanced in the momentum equations. For this, we calculate (Fig. 3) their depth-averaged cross-shore and alongshore values, integrated between t_0 the beginning of the simulation and t_1 the time when the simulation becomes stationary. Velocities are dependent on these values:

$$\hat{\boldsymbol{u}}(t_1) = \int_{t_0}^{t_1} \left[\boldsymbol{F}_{\text{wave}} + \boldsymbol{F}_{\text{other}}\right] dt + \underbrace{\hat{\boldsymbol{u}}(t_0)}_{=0}. \tag{28}$$

Wave-induced forces are $\boldsymbol{F}_{\text{wave}}$ and other forcings are $\boldsymbol{F}_{\text{other}}$. Thus, the surface stress τ_{wo} is converted into a vertically averaged acceleration. We do not display the bottom stress because in this case we have fixed the value of the drag coefficient and assume that waves do not directly modify the bottom stress. Besides, the Stokes-Coriolis force is not represented because rotation is excluded. A test with a non-null Coriolis parameter showed that the Stokes-Coriolis force is negligible in this scale.

The alongshore forcing is the result of two predominant forces: the vortex force and the surface stress. The surface stress drives the northward velocities. In fact, until x reaches 700 m, the vortex force is oriented southward, tending to compensate the surface dissipation. Thereafter it becomes positive and is oriented northward. It adds to the surface stress for the generation of an alongshore jet. The balance between the vortex force and the surface stress is thus responsible for the cross-shore position of the jet peak. The vortex force is maximal at the surface (because Stokes velocities are maximal at the surface) so the balance tends to be reached for every vertical level, explaining the uniformity of the alongshore velocity with depth. In the surf zone for

OSD
8, 2417–2478, 2011

$x > 950$ m, both the surface stress and the vortex force are oriented southward inducing the longshore velocity to decrease near the shoreline. The cross-shore forces are two orders of magnitude larger than the alongshore ones. The most important is the surface stress but this is concentrated in the surf zone, directing the surface cross-shore velocity to the shoreline. The second most important force, smaller in size by an order of magnitude, is the depth-uniform pressure gradient. This force indirectly acts on the surface elevation. When waves shoal before the surf zone, the pressure gradient is negative, creating a set-down. As it turns positive, a set-up is generated. The depth-integrated cross-shore vortex force is negligible, but this force is strongly vertically sheared due to the vertical profiles of the Stokes velocities. It thus appears that the vertical profile of the velocities is widely dependent on the surface stress and how this momentum penetrates into the vertical column, as well as the vertical profile of the vortex force which is related to the profile of the Stokes velocities.

3.1.2 Sensitivity tests considering the effects of surface conditions on vertical mixing and surface roughness

As we have seen before, vertical shear is highly related to the vertical mixing. In this section, we test different surface boundary conditions in the parameterization of the turbulence closure. In the reference simulation, eddy viscosity was parameterized according to Gaspar et al. (1990). At the surface, we add the condition of Craig and Banner (1994) (Eq. 18). Furthermore, for these two parameterizations, we test different mixing lengths / (Eq. 20). In the reference simulation, the surface roughness was fixed to 0.015 m. We therefore tested values between 0.8 and 2.4 H_s as in Rascle et al. (2006).

The parameterization of Craig and Banner (1994) adds a flux of energy and increases the vertical mixing. Consequently, the vertical shear is less marked (Fig. 4b) between $500 < x < 1000$ m, thus the depth integrated alongshore velocity is increased in the surf zone (Fig. 4a). These results are in agreement with the results of HW09. In this approach, there was no addition of a surface stress linked to waves, so currents

OSD
8, 2417–2478, 2011

were not sheared as in UMS10's results. When the mixing length is related to the significant wave height, alongshore velocities are again increased, and the peak is moved offshore. The larger the mixing length, the more uniform the velocities are with depth and the less important the shear is. Our results agree with the previous simulations performed by other models using different theories. The littoral drift and vertical profiles are correctly reproduced by our model. Nevertheless, the sensitivity tests and the analysis show that these profiles are highly dependent on the vertical mixing and the surface penetration of the Stokes velocities. Even if the model is in agreement with the others, a comparison with in situ data or laboratory measurements is necessary to assess whether the 3-D characteristics are accurate (Sects. 3.2 and 4).

3.2 A barred beach with rip current

The purpose of this test case is to check the ability of the model to correctly reproduce the rip current phenomena, before tackling the study of the complex sandbar systems of the Têt inner shelf. We reproduce test B experiments of Haller et al. (2002) performed in the basin of the Ocean Engineering Laboratory (University of Delaware). Previous modelers have reproduced this experiment with the SHORECIRC model Haas et al. (2003), with the MARS model Bruneau (2009), and also with the ROMS using the wave forcing radiation stress approach of Haas and Warner (2009). The size of the modeled basin is 15.8 m in the cross-shore direction x and 18.6 m in the alongshore direction y. Between 1.5 m and 3 m from the wave maker, the beach slope is steep (1:5) but it is mild (1:30) for the rest of the domain. A longshore bar system made up of three bars of 7.32 m in length and 6 cm in height, separated by rip channels of 1.82 m, is located at 6 m from the coast. The grid spacing is similar to Haas et al. (2003), and is 20 cm in the horizontal direction. Seven vertical levels are used. Lateral periodic conditions are stipulated and rotation is excluded. Eddy viscosity is parameterized according to Gaspar et al. (1990), and the condition of Craig and Banner (1994) is not specified at the surface. At the bottom, we use the Eq. (14) for the boundary condition.

OSD
8, 2417–2478, 2011

The wave forcing is performed by SWAN. A monochromatic wave is imposed at the offshore edge with a 0.0724 m significant wave height and 1 s peak period, perpendicular to the direction of the beach (top of Fig. 5). Waves break suddenly over the bar while being more progressive through the rip channel. There is a little shoaling before the breaking point above the bar, but it is insignificant through the rip channel. As previously noted by Haas et al. (2003) and Weir et al. (2011), this is because there is no forcing by the current on the waves. Besides, Weir et al. (2011) have shown that rip currents reduce the flux of momentum from waves to currents due to wave breaking. However, this modification can be parameterized in a model without current effects on waves, by enhancing the bottom friction law (Weir et al., 2011). So the choice of the drag coefficient is crucial to obtain a current similar to the observations. In addition, the stationary or non-stationary state of the simulation strongly depends on this coefficient. Actually, laboratory experiments and previous numerical simulations (Haas et al., 2003; Haas and Warner, 2009) have noticed that rip currents are unstable flows. We observe the same features in our simulation. In order to reduce the instabilities in the simulations and to facilitate the comparison with the time-averaged measurements, it is recommended to increase the friction factor. With a quadratic bottom drag law with a drag coefficient equal to 0.005, our simulation becomes stationary after 10 min.

Here we do not go into details of this experiment. A study focused on rip currents would have required more sensitive tests, considering the roughness, the current forcing on waves, the roller influence, etc. The reader is invited to refer to Weir et al. (2011) for a more detailed vortex force analysis of the rip current. The aim here is only to check the ability of the model to qualitatively and quantitatively reproduce the observed phenomena. Two recirculation cells of currents are generated by the wave forcing (Fig. 6): one in the surf zone with currents oriented shoreward over the bars and offshore above the channels, and another less marked between the bars and the shoreline. This second recirculation cell is made up of the excess of water brought by waves waiting to be evacuated offshore via the channels. These two patterns are observed both in simulations and in experiments. Intensities of depth-integrated currents fit with the data, with

OSD
8, 2417–2478, 2011

a maximum value equal to 0.25 m s^{-1}. The consistency of the current vertical profiles is difficult to check because no 3-D-measurements were performed in the experiment. They are difficult to obtain in general because of the sporadic and changing nature of currents in these kinds of systems. Nevertheless, some indications and observations are available: Haas and Svendsen (2002) point out that above channels currents are uniform in the vertical column. On the contrary, offshore, strong surface currents directed offshore are visible in the upper part of the water column, contrasting with lower velocities near the bottom, directed either offshore or shoreward, depending on the volume flux brought in by the waves. In our simulation (Fig. 7), cross-shore velocities are stronger in the channel than above the bar. Downstream from the channel, vertical profiles are the most strongly sheared, with a strong current directed offshore at the surface, and weak velocities at the bottom. Along the cross-shore direction above the middle bar, it is only on the bar that the cross-shore velocity is non-null but extremely sheared: the current is oriented onshore close to the surface and the bottom, and offshore elsewhere. This simulation agrees well with the observations of Haas and Svendsen (2002), so the study considering the real case can be tackled with some confidence.

4 Application to 21 February 2004 storm at the Têt inner shelf

4.1 General context

4.1.1 Coastal circulation and the Têt system

The Têt River discharges into the Southwestern part of the Gulf of Lion (hereinafter GoL) in the Northwestern Mediterranean Sea (Fig. 8). Circulation in this micro-tidal zone in front of this river is strongly controlled by wind conditions. Estournel et al. (2003) and Ulses et al. (2008a) show that two major winds, the Tramontane (NW) and Marin (SE), induce cyclonic circulation in the GoL generating a southward current

OSD
8, 2417–2478, 2011

along the Têt coast. During East or South-East storms, this general counterclockwise circulation is intensified in the inner shelf but is opposed by an alongshore Northward littoral drift. Evidence of this drift has been provided by Anguenot and Monaco (1967) with radioactive tracers, by Delpont and Motti (1994) with aerial and SPOT images, multidate Remote Sensing by Certain (2002) and by Bourrin et al. (2008), who analyzed bathymetric and sediment data.

The Têt is a small river with an average water discharge of less than $10\,m^3\,s^{-1}$, with exceptional peaks two orders of magnitude higher during high precipitation events (Serrat et al., 2001). The littoral zone, where it discharges, has a complex bathymetry. A recent LiDAR (Light Detection and Ranging) survey (Fig. 9) shows a sand spit developing northwards of the breakwaters of the Canet-en-Roussillon harbor, followed by a deep pit, as observed by Bourrin et al. (2008). Thereafter, complex double crescentic sandbar systems, classified as Low Tide Terraces (LTT) by Aleman et al. (2011), are observed. They appear chaotic and are likely disturbed by the breakwaters of the harbour and the river. The internal bars have their left side more onshore than their right side, suggesting that they have been modified by the northward littoral drift.

4.1.2 Instrumental devices

As part of the Eurostrataform program (Weaver et al., 2006), a field observation program was conducted from November 2003 to April 2004 in order to characterize the sediment transfer from the river to the slope, then to the open ocean. Meteorological, sedimentological and hydrodynamic data were collected. The wind field was measured every 1 h at the Meteo-France Toreilles meteorological station located 8 km further north of the Têt mouth. A 600 kHz Teledyne RDI Sentinel ADCP, equipped with a wave gauge, was deployed on the inner shelf at a depth of 28 m and 2 km from the river mouth (POEM point, position: 42°42.25′ N, 03°04.01′ E, Fig. 8). It collected wave and current data between 26 November 2003 and 16 January 2004 and between 4 February and 26 March 2004. The sampling rate was set to 20 mn every 3 h at 2 Hz for wave measurements and currents were measured at 1.5 Hz between the wave measurement

OSD
8, 2417–2478, 2011

bursts. The ADCP was set in a trawl bottom mount and turned toward the surface to record currents with 23 cells of 1 m of resolution. Between 11 February 2004 and 21 June 2004, an Acoustic Doppler Profiler (ADP) Nortek AWAC was positioned at a depth of 11 m (SODAT point, position: 42°43.23′ N, 03°02.89′ E) (Fig. 8) in front of the Têt river, in order to measure the current as well as waves (using a wave pressure sensor) every 30 min. The ADP was set on the sea bottom and looked upward, with 9 cells of 1 m. Lastly, between 11 February 2004 and 14 January 2005, a 600 kHz Aquadopp Profiler, located at a depth of 31 m (SOPAT point, position: 42°42.59′ N, 03°04.78′ E) (Fig. 8), measured current profiles every 5 min with cells of 2 m. It was fixed to a buoy, looking downward.

4.1.3 The storm of 21 February 2004

During the sampling period, two major storms occurred, one on 4 December 2003 and another on 21 February 2004 (Guillén et al., 2006). We focus on the second storm since more data are available for this period. The storm was characterized at SOPAT by a maximum significant wave height $H_s > 7$ m and a peak period $T > 12$ s, with a westward peak direction (Guillén et al., 2006). At SODAT, significant wave height reached 6 m at 05:00 a.m. (Figs. 11 and 12) while the wind blew out of the south-east and reached up to 16 m s^{-1} (Fig. 10). The water and sediment discharge of the Têt, as estimated by Guillén et al. (2006), were very low compared to the previous storm (only 450 t of sediment compared to 20 000 t in December). Wind and wave were thus the predominant forcing during this storm. According to Guizien (2009), the return period for both storms was 10.5 yr at Sète (located 100 km to the north-east) and 5 yr at Banyuls (located 20 km further south). Before and after the storm, the current was southward at SODAT (11 m) (Figs. 13, 14), with low intensity (<10 cm s^{-1}). At the beginning of the day (21 February), the direction of the current at SODAT turned toward the north, and the current increased in intensity to reach approximately 90 cm s^{-1} throughout the water column at 04:00 a.m. of the same day. Its intensity remained high, but then began to decrease after 4 h, remaining at moderate intensity (around 20 cm s^{-1}) for 30 h while

OSD
8, 2417–2478, 2011

the direction turned southward. At POEM (28 m) and SOPAT (31 m) (Figs. 13, 14), the current was generally oriented southward. During the storm, when wind strengthened, it increased reaching about 50 cm s^{-1} at the surface, and 40 cm s^{-1} near the bottom. At these two offshore stations, the current remained abnormally strong (>15 cm s^{-1}) for more than 50 h.

4.2 Implementation and results

We aim to accurately reproduce phenomena induced by waves and current, covering scales from the whole Western Mediterranean Sea to the Têt nearshore zone. A first attempt consisted of using four nested grids for the hydrodynamic circulation model (with grid resolutions between 2.5 km and 15 m). Using this set up, spurious flows were observed near the shoreline at the northern boundary of the finest grid. This was due to the representation of the littoral drift that strongly depends on the resolution of the model. As pointed out by Davies and Jones (1996), one solution is to use an unstructured grid or a grid with a variable resolution, that covers the entire Têt inner-shelf, with a fine resolution at the Têt mouth which is gradually reduced to a coarser resolution in offshore zones. Using such grids ensures a smooth transition between offshore and nearshore zones. We choose this second approach here.

4.2.1 Wave model implementation and results

We use three nested grids to model the sea state, two structured grids that cover the whole Western Mediterranean Sea and the Gulf of Lion, respectively, and an unstructured grid, which runs from the inner-shelf with a resolution of 550 m at the offshore boundaries to the surf zone of the Têt (Fig. 8 and Table 1). The size of the cells is 22 m near the Têt mouth. The grid is made of 64 000 nodes and 127 500 elements.

Simulations are run with WW3 for a period of two months, from 4 February to 26 March 2004 (the period for which observations are available). We use the TEST405 parameterizations as described in Ardhuin et al. (2010) which are more adapted for the

OSD
8, 2417–2478, 2011

younger seas that occur in the Mediterranean Sea. The wind velocities are provided by the Aladin model (a regional weather forecasting model focused on France with a resolution of 10 km) from Météo-France every 3 h, except for WW3-MEDOC where Aladin is supplemented by Arpege (a global atmospheric model from Météo-France with a grid resolution of 15 km over France). Output wave spectra are discretized over 36 directions with 10°of resolution and 30 frequencies f_n spaced with the relation $f_{n+1} = 1.1\, f_n$ from 0.05 Hz to 0.8 Hz. Bathymetry in the Têt surf zone is complex and the length of sand bars ranges between 200–300 m. To correctly reproduce the wave breaking, and consequently the wave-induced current, it is necessary to simulate the waves with a resolution coherent with the size of the bars. A resolution of 22 m is used near the Têt in this study.

We compare the wave model results to the significant wave heights and wave periods recorded by the two wave gauges (SODAT and POEM) during the winter campaign (Figs. 11 and 12) and by analyzing the statistical values of correlation coefficient (COR), bias (BIAS), root mean square error (RMSE) and scatter index (SI). If N is the number of observed and simulated values, S_i the simulated values, O_i the observed values, S and O the mean of simulated and observed values, respectively, then the statistical values are:

$$\begin{cases} \mathrm{COR} = \dfrac{\sum_{i=1}^{N}(S_i-\overline{S})(O_i-\overline{O})}{\sqrt{\sum_{i=1}^{N}(S_i-\overline{S})^2 \sum_{i=1}^{N}(O_i-\overline{O})^2}} \\ \mathrm{BIAS} = \overline{S}-\overline{O} \\ \mathrm{SI} = \sqrt{\dfrac{\sum_{i=1}^{N}(S_i-O_i)^2}{\sum_{i=1}^{N}(S_i)^2}} \\ \mathrm{RMSE} = \sqrt{\dfrac{\sum_{i=1}^{N}(S_i-O_i)^2}{N}} \end{cases} \quad (29)$$

Statistical results show a good agreement between the two datasets and the simulation (Table 2). For example, a correlation of 93 % is found for the significant wave height at POEM and 96 % at SODAT. During the storm period (Figs. 11 and 12), the

OSD
8, 2417–2478, 2011

three parameters fit well. We note, however, that significant wave heights are slightly underestimated by the model (Fig. 12), with a bias of 20 cm at the storm apex and especially during the afternoon, with a bias of 1.5 m. We performed sensitivity tests with different atmospheric models for the storm event and, depending on the models or the period, wave heights are under or overestimated. A comparison between wind intensity measured at the Toreilles meteorological station and the one simulated at SODAT (Fig. 10) shows that the Aladin model is in reasonable agreement with the data especially if we consider that a comparison between two data sets, one on land and one over the sea, is biased. Besides, the time-averaged nature of the model does not allow to reproduce the strong effect of gusts acting during the storm period. Finally, observations and simulations both indicate that significant wave height decays between the two sites, suggesting that wave dissipation on the bottom occurs in the inner shelf zone.

4.2.2 Current model implementation

As for the wave model, three nested grids for the circulation model are deployed, with the focus towards the Têt nearshore (Fig. 8). All details concerning the different grids are presented in Table 3. Grid TET is a stretched curvilinear horizontal grid with a variable horizontal resolution (Madec, 2008), from 8×8 m at the nearest grid point from the Têt mouth to 180×180 m offshore. Bathymetries from Berné et al. (2002) and from the LiDAR for the nearshore are used. As explained above, a high resolution near the river mouth is necessary in order to reproduce all current patterns generated by the crescentic sandbars that impacted the SODAT instrument. Daily river discharges were provided by Banque Hydro and Compagnie Nationale du Rhone (http://www.hydro.eaufrance.fr/). The meteorological forcings (surface pressure, air temperature, relative humidity, wind velocity and radiative fluxes) are taken from the Aladin model every 3 h. The regional circulation model (grid MEDOC) is initialized and forced every day by the large-scale Ocean General Circulation Model (OGCM, Tonani et al., 2008). The wave forcing is not been taken into account in the circulation model at the regional scale

OSD
8, 2417–2478, 2011

(MEDOC) but at all other scales, every 3 h for the GoL, and every 1 h for TET. The roughness length is set to 1 cm throughout the domain.

4.2.3 Hydrodynamic results and discussion

Importance of the wave forcing

Firstly, a simulation without wave forcing (Figs. 13, 14) is performed. All other forcing terms are present, including the wind and the larger scale circulation. Simulated currents are very small, and neither littoral drift nor rip currents are observed. At SODAT (11 m), current intensity is 0.17 m s^{-1} close to the surface and near the bottom. It is directed southward throughout the water column. This value is not consistent with the measured values. At POEM (28 m) and SOPAT (31 m), currents are stronger but they are also underestimated compared to the data during the first hours of the storm. On the afternoon of 21 February, simulated intensities reach less than half of the measured intensities. Ulses et al. (2008b) simulated the inner shelf for this period without the wave forcing, and noticed that currents were also underestimated.

Current in the surf zone

At the beginning of the storm, waves propagate from the east, with the irregularities of the bathymetry creating alongshore variations in breaking wave heights (Fig. 15), which in turn are responsible for the complex recirculation cells (Fig. 16, top) and oscillating meanders in the surf zone and on the inner shelf (Bowen, 1969). These types of meanders are often observed (e.g. Reniers et al., 2001) at Palm Beach in Australia. In fact, when waves have a near normal angle of incidence, we have seen in Sect. 3.2 for the second test case, that over a bathymetry made of bars and channels, the current is dominated by a rip-current flow and not a longshore drift. This is what we observe here (Fig. 16, Sects. 1 and 2). A bar, at a depth of 2.5 m in Sect. 1, is able to break waves and generates a strong feeder current that circulates through to the beach and exits offshore near Sect. 2, where the breaking bar is too close to the shore to break

OSD
8, 2417–2478, 2011

waves. The rip current dynamics are more complex than in the test case, and largely influenced by the Canet harbour tip. Vertical sections show that over the breaking bar (Sect. 1, Fig. 17), cross-shore velocities are stronger close to the surface (>0.8 m s^{-1}) and directed onshore almost everywhere. Above the channel (Sect. 2, Fig. 17), current is oriented seaward everywhere, and is stronger in the middle of the water column.

On 21 February around 02:00 a.m., the incident direction turns and breaking waves arrive at the coast obliquely from the East-South-East. They create a longshore northward drift almost everywhere in the surf zone near the river mouth (Fig. 16, bottom). But this flow is not regular and is perturbated by the bathymetry and the remaining circulation. A recirculation cell is, for example, observed at the 42° 42′45″ N latitude. This kind of phenomenon was observed first by Oltman-Shay et al. (1989) and explained by Ozkan-Haller and Kirby (1999): in the presence of waves and when a current is strongly sheared, the meanders can grow and form eddies that either move along with the current, or are ejected offshore, forming rip currents. In addition, originally from the south, the longshore drift is getting stronger and pushed offshore as a result of the southern tips of the harbours. These results are consistent with the development of sand spits growing northwards at river mouths, sand bars and harbours, as observed by Delpont and Motti (1994); Bourrin et al. (2008) and in the LiDAR bathymetry. Downstream of the harbour, a cyclonic eddy and a return current along the northern breakwater of the harbour are generated, as discussed by Trampenau et al. (2004). These phenomena explain the strong erosion observed here and in general along the harbour side in the lee of the waves (Trampenau et al., 2004). Going to the north, after the harbour, the drift is confined in a narrow zone along the 10 m isobath because of the wave effect. The Têt discharge and some remaining rip currents also move the drift offshore. Further northwards of the river mouth, the drift is finally able to spread to the shoreline, decreasing in intensity. The direction of the drift is not as simple as in the first test case, and vertical profiles of current are difficult to analyse because recirculation, rip currents and littoral drift are present and interact. In the drift, however, current is quite uniform with depth (Fig. 14, top and Fig. 18).

OSD
8, 2417–2478, 2011

We compare the simulated currents with the measured currents at SODAT (Figs. 13, 14). Before the storm event, simulated currents are weak and oriented southward. In the first hours of the storm, due to the angle of wave incidence, a rip current running by SODAT and oriented to the east (Figs. 14 and 16), is simulated with intensities reaching 90 cm s^{-1} close to the surface. An eastward current is also measured but recorded intensities are very weak (<20 cm s^{-1}). This rip current has a narrow width, and it may be possible that in reality, the instrument is not exactly in the area where the rip current is acting. In fact, this area is highly dependent on the bathymetry, and the discrepancy between model and data may result from the fact that the modelled bathymetry is built from the LiDAR survey conducted in 2008, four years after this studied storm. At the storm peak, current turns towards the north-east, reaching 85 cm s^{-1} at the surface and 75 cm s^{-1} at the bottom. Thereafter, its intensity decreases and its orientation returns southward as before the storm. Orientation and intensity fit very well with the data. Near the bottom, however, the simulated current is slightly underestimated (75 cm s^{-1} against 85 cm s^{-1} in the reality). The misrepresentation of the bedforms contributes to increase the error on the roughness of the model, which largely influences the bottom current. A sensitivity test was performed and proved that the drift intensity in the entire water column was increased when the roughness was decreased. But as the drift is not regular, its position also moves when changing a parameter: the general pattern of the drift is preserved, but its location varies as well as the secondary circulation cells. The same observation is also made when the surface roughness length, and in consequence, the vertical mixing is changed. It is extremely difficult to assess the impact of such parameters with only one instrument in a realistic surf zone and in real conditions.

Current on the inner shelf

On the whole inner shelf, from a depth of 25 m, simulated currents are southward during the entire simulation and intensify during the storm.

OSD
8, 2417–2478, 2011

At POEM (28 m), the simulated currents are stronger with the wave forcing than without (middle of Figs. 13, 14): they reach 40 cm s^{-1} at the surface and 20 cm s^{-1} near the bottom, instead of 30 cm s^{-1} at the surface and 25 cm s^{-1} near the bottom without the wave forcing. At the beginning of the storm, close to the surface, the simulated current fits the data, but in the beginning of the afternoon, simulated currents are weaker than the observed currents. In fact, we noted previously that the modeled wave heights decrease too soon compared to the observed ones, which results in a shorter duration of storm. In addition, near the bottom, the simulated current strongly underestimates the measured one. Similarly, at SOPAT (31 m), currents reach 55 cm s^{-1} at the surface and 18 cm s^{-1} near the bottom (instead of 30 cm s^{-1} close to the surface and 18 cm s^{-1} near the bottom without the wave forcing). They reproduce the observed currents in the first hours of the storm, but also underestimate them thereafter. The discrepancy between model results and observations may be explained by an underestimation of the wind speed, as we previously pointed out when describing the wave model results. A test where we increase the wind speed by a factor of 1.2, shows that in the surf zone and at SODAT, results are unchanged, but on the inner shelf (and especially at SOPAT and POEM), current intensities reach the observed values at the surface, and are increased in the entire water column. Either the atmospheric model underestimates wind speed over the sea during storms, or the calculation of the surface stress is not correct for a young sea. This sensitivity test also reveals that circulation on the inner shelf is highly dependent on the atmospheric forcing and the global circulation whereas in the surf zone, processes linked to waves are the most important.

5 Conclusions

We have developed and implemented a new method to take into account the impact of waves on the 3-D circulation. This method can be used from the nearshore to the global scale. It is first tested on two classical academic cases. Results fit with previous simulations performed by other models and with available observational data.

OSD
8, 2417–2478, 2011

A realistic case of energetic waves arriving at a coast of the northwest Mediterranean for which currents were available at different depths as well as an accurate bathymetric database of the 0–10 m depth range, was then simulated. A grid nesting approach was used to account for the different forcings acting at different spatial scales. The simulation coupling the effects of waves and currents is successful to reproduce the powerful northward littoral drift in the 0–15 m depth zone while without waves, the current is slow in the opposite direction. More precisely, two distinct cases were identified: when waves have a normal angle of incidence with the coast, they are responsible for complex circulation cells and rip currents in the surf zone, and when they travel obliquely, they generate a northward littoral drift. These features are more complicated than in the test cases, due to the complex bathymetry and the consideration of wind and non-stationary processes. Wave impacts in the inner shelf are less visible since wind and regional circulation seem to be the predominant forcings. Besides, the discrepancy between model and observations is noted at that scale, possibly linked to the underestimation of the wind stress. A perspective of this study could be to fully couple wave and circulation models to estimate the potential effect of current on wave properties through blocking or refraction itself impacting the circulation through modification of the water level.

Lastly, during storm events, a classical sediment transport approach without wave forcing (e.g. Ulses et al., 2008b) does not permit the reproduction of either the northward transport in the surf zone or the transport of large amount of fine particles discharged most of the time during events combining high waves and floods. Moreover, the bottom shear stress would be strongly underestimated and then, also the possibility of resuspension for coarse sediment. In the specific case of the region studied here, we expect to extend the study of Ulses et al. (2008b) on the impact of storms on the sediment transport at regional scale to the nearshore zones. We will be then able to study the fate of sediments ranging from the river and the beach to the open ocean and so complete the study undertaken by Palanques et al. (2011).

OSD
8, 2417–2478, 2011

Acknowledgements. We thank Y. Uchiyama and J. C. Warner for sharing the SWAN model data and for discussions. We thank the DREAL of Languedoc Roussillon for the LiDAR bathymetry, Xavier Durrieu de Madron (CEFREM, Perpignan), Safege-Cetiis for the in-situ data and the post-treatment. We warmly thank Cyril Nguyen and the POC crew for their assistance and Fiona Tummon for her proofreading. We acknowledge Meteo-France for the ALADIN and ARPEGE for the model outputs. We thank also MOON (the Mediterranean operational oceanography network) for OGCM outputs. This study was supported by the GMMC (groupe mission mercator coriolis). H. M. is financially supported by the CNRS and the Languedoc-Roussillon Region. F. A. is supported by a FP7-ERC young investigator grant number 240009 for the IOWAGA project. This work is also a contribution to the EPIGRAM project, funded by CNRS (national programm LEFE/IDAO) and ANR (grant ANR-08-BLAN-0330-01). The Symphonie ocean model is developed by the SIROCCO group. Sources are available at http://sirocco.omp.obs-mip.fr/outils/Symphonie/Sources/SymphonieSource.htm.

The publication of this article is financed by CNRS-INSU.

References

Agrawal, Y. C., Terray, E. A., Donelan, M. A., Hwang, M. A., Williams III, A. J., Drennan, W. M., Kahma, K. K., and Kitaigorodskii, K. K.: Enhanced dissipation of kinetic energy beneath surface waves, Nature, 359, 219–233, 1992. 2419

Aleman, N., Robin, N., Certain, R., Vanroye, C., Barusseau, J., and Bouchette, F.: Typology of nearshore bars in the Gulf of Lions (FRANCE) using LIDAR technology, J. Coastal Res., 64, 721–725, 2011. 2439

Andrews, D. and McIntyre, M.: An exact theory of non-linear waves on a Lagrangian mean flow, J. Fluid Mech., 89, 609–646, 1978. 2420, 2421

OSD
8, 2417–2478, 2011

Anguenot, F. and Monaco, A.: Etude des transits sédimentaires sur le littoral du Roussillon par la méthode des traceurs radioactifs, Cahiers Océanographiques, 19, 579–589, 1967. 2439
Ardhuin, F., Chapron, B., and Elfouhaily, T.: Waves and the Air-Sea Momentum Budget: Implications for Ocean Circulation Modeling, J. Phys. Oceanogr, 34, 1741–1755, 2004. 2426
Ardhuin, F., Jenkins, A. D., and Belibassakis, K. A.: Comments on "The Three-Dimensional Current and Surface Wave Equations", J. Phys. Oceanogr., 38, 1340–1350, doi:10.1175/2007JPO3670.1, 2008a. 2420
Ardhuin, F., Rascle, N., and Belibassakis, K.: Explicit wave-averaged primitive equations using a generalized Lagrangian mean, Ocean Modell., 20, 35–60, doi:10.1016/j.ocemod.2007.07.001, 2008b. 2418, 2419, 2420, 2421
Ardhuin, F., Collard, F., Chapron, B., Queffeulou, P., Filipot, J.-F., and Hamon, M.: Spectral wave dissipation based on observations: a global validation, in: Proceedings of the chinese-german joint symposium on hydraulic and ocean engineering, edited by: Zanke, U., Roland, A., Saenger, N., Wiesemann, J. U., and Dahlem, G., 391–400, Chinese-German Joint Symposium on Hydraulic and Ocean Engineering, Darmstadt, Germany, 24–30 August 2008, 2008c. 2431
Ardhuin, F., Mari, L., Rascle, N., Forget, P., and Roland, A.: Observation and estimation of Lagrangian Stokes and Eulerian currents induced by wind at the sea surface, J. Phys. Oceanogr., 39, 2820–2838, 2009. 2419
Ardhuin, F., Rogers, E., Babanin, A. V., Filipot, J., Magne, R., Roland, A., van der Westhuysen, A., Queffeulou, P., Lefevre, J., Aouf, L., and Collard, F.: Semiempirical Dissipation Source Functions for Ocean Waves. Part I: Definition, Calibration, and Validation, J. Phys. Oceanogr., 40, 1917–1941, doi:10.1175/2010JPO4324.1, 2010. 2418, 2425, 2431, 2441
Bennis, A. and Ardhuin, F.: Comments on "The Depth-Dependent current and Wave Interaction Equations: A Revision", J. Phys. Oceanogr., accepted, 2011. 2420
Bennis, A., Ardhuin, F., and Dumas, F.: On the coupling of wave and three-dimensional circulation models: Choice of theoretical framework, pratical implementation and adiabatic tests, Ocean Modell., 40, 260–272, 2011. 2418, 2421, 2422, 2423, 2424, 2426, 2427
Berné, S., Satra, C., Alosi, J., Baztan, J., Dennielou, B., Droz, L., Reis, A. D., Lofi, J., Méar, Y., and Rabineau, M.: Carte morpho-bathymétrique du Golfe du Lion, notice explicative, Institut français de recherché pour l'exploitation de la mer (IFREMER), Brest, France, 2002. 2443
Blumberg, A. and Mellor, G.: A description of a three-dimensional coastal ocean circulation model, in: Three-dimensional Coastal Ocean Models, edited by: Mooers, C. N. K., Coast.

OSD
8, 2417–2478, 2011

Est. S., 4, 1–16, 1987. 2424
Booij, N., Ris, R., and Holthuijsen, L.: A third generation wave model for coastal regions, part 1: model descritpion and validation, J. Geophys. Res., 104, 7649–7666, 1999. 2418, 2427, 2431
Bougeault, P. and Lacarrere, P.: Parameterization of orography induced turbulence in a mesobeta-scale model, Mon. Weather Rev., 117, 1872–1890, 1989. 2422, 2428
Bourrin, F., Friend, P., Amos, C., Manca, E., Ulses, C., Palanques, A., de Madron, X. D., and Thompson, C.: Sediment dispersal from a typical Mediterranean flood: The Têt River, Gulf of Lions, Cont. Shelf Res., 28, 1895–1910, doi:10.1016/j.csr.2008.06.005, 2008. 2439, 2445
Bowen, A.: Rip currents: 1.Theoretical investigations, J. Geophys. Res., 74, 5467–5478, 1969. 2444
Bruneau, N.: Modélisation morphodynamique des plages sableuses, Ph.D. thesis, Université Bordeaux I, 2009. 2431, 2436
Certain, R.: Morphodynamique d'une côte sableuse microtidale à barres: le Golfe du Lion (Languedoc-Roussillon), Ph.D. thesis, Université de Perpignan, 2002. 2439
Chawla, A. and Kirby, J.: Monochromatic and random wave breaking at blocking points, J. Geophys. Res., 107, 3067, doi:10.1029/2001JC001042, 2002. 2420
Chen, Q., Kirby, J. T., Dalrymple, R. A., Fengyan, S., and Thornton, E. B.: Boussinesq modeling of longshore currents, J. Geophys. Res.-Oceans, 108, 1–24, 2003. 2419
Clark, D., Feddersen, F., and Guza, R.: Boussinesq modeling of surfzone tracer plumes, part 2: Tracer plumes and cross-shore dispersion, J. Geophys. Res., 116, C11028, doi:10.1029/2011JC007211, 2011. 2419
Craig, P. D. and Banner, M. L.: Modeling Wave-Enhanced Turbulence in the Ocean Surface Layer, J. Phys. Oceanogr., 24, 2546–2559, 1994. 2428, 2435, 2436, 2464
Davies, A. and Jones, J. E.: Sensitivity of tidal bed stress distributions, near bed currents, overtides and tidal residuals to frictional effect in the eastern Irish Sea, J. Phys. Oceanogr., 26, 2553–2575, 1996. 2441
Delpey, M. T., Ardhuin, F., Collard, F., and Chapron, B.: Space-time structure of long ocean swell fields, J. Geophys. Res.-Oceans, 115, C12037, doi:10.1029/2009JC005885, 2010. 2431
Delpont, G. and Motti, E.: Monitoring by remote sensing of the geomorphological evolution of a part of the Roussillon coastal layout (France), Oceanis 94 Osates, 44–47, 1994. 2439, 2445
Donelan, M., Dobson, F., and Smith, S.: On the dependance of sea surface roughness on wave

OSD
8, 2417–2478, 2011

development, J. Phys. Oceanogr., 23, 2143–2149, 1993. 2419
Dufois, F.: Modélisation du transport particulaire dans le Golfe du Lion en vue d'une application au devenir des traceurs radioactifs issus du Rhône, Ph.D. thesis, Université du Sud Toulon-Var, 2008. 2431
Estournel, C., Broche, P., Marsaleix, P., Devenon, J., Auclair, F., and Vehil, R.: The Rhone river plume in unsteady conditions: Numerical and experimental results, Estuar. Coast. Shelf S., 53, 25–38, 2001. 2429
Estournel, C., Durrieu de Madron, X., Marsaleix, P., Auclair, F., Julliand, C., and Vehil, R.: Observation and modeling of the winter coastal oceanic circulation in the Gulf of Lion under wind conditions influenced by the continental orography (FETCH experiment), J. Geophys. Res., 108, 8059, doi:10.1029/2001JC000825, 2003. 2422, 2438
Estournel, C., Zervakis, V., Marsaleix, P., Papadopoulos, A., Auclair, F., Perivoliotis, L., and Tragou, E.: Dense water formation and cascading in the Gulf of Thermaikos (North Aegean), from observations and modelling, Cont. Shelf Res., 25, 2366–2386, doi:10.1016/j.csr.2005.08.014, 2005. 2422
Estournel, C., Auclair, F., Lux, M., Nguyen, C., and Marsaleix, P.: "Scale oriented" embedded modeling of the North-Western Mediterranean in the frame of MFSTEP, Ocean Sci., 5, 73–90, doi:10.5194/os-5-73-2009, 2009. 2422
Flather, R.: A tidal model of the northwest european continental shelf, Mémoires, Société Royale des Sciences de Liège, 6, 10, 141–164, 1976. 2427
Garrett, C.: Generation of Langmuir circulations by surface waves – a feedback mechanism, J. Mar. Res., 34, 117–130, 1976. 2420
Gaspar, G., Gregoris, Y., and Lefevre, J.: A simple eddy-kinetic-energy model for simulations of the ocean vertical mixing: tests at station papa and long-term upper ocean study site., J. Geophys. Res., 95, 16179–16193, 1990. 2426, 2428, 2435, 2436, 2464
Guillén, J., Bourrin, F., Palanques, A., de Madron, X. D., Puig, P., and Buscail, R.: Sediment dynamics during wet and dry storm events on the Têt inner shelf (SW Gulf of Lions), Mar. Geol., 234, 129–142, 2006. 2440
Guizien, K.: Spatial variability of wave conditions in the Gulf of Lions (NW Mediterranean Sea), Vie Milieu, 59, 261–270, 2009. 2440
Haas, K. A. and Svendsen, I. A.: Laboratory measurements of the vertical structure of rip currents, J. Geophys. Res., 107, C5, doi:10.1029/2001JC000911, 2002. 2438
Haas, K. A. and Warner, J. C.: Comparing a quasi-3D to a full 3D nearshore circulation model:

OSD
8, 2417–2478, 2011

SHORECIRC and ROMS, Ocean Modell., 26, 91–103, 2009. 2418, 2421, 2422, 2432, 2436, 2437

Haas, K. A., Svendsen, I. A., Haller, M., and Zhao, Q.: Quasi-three-dimensional modeling of rip current systems, J. Geophys. Res., 108, 3217, doi:10.1029/2002JC001355, 2003. 2436, 2437, 2466

Haller, M., Dalrymple, R., and Svendsen, I. A.: Experimental study of nearshore dynamics on a barred beach with rip channels, J. Geophys. Res., 107, C6, doi:10.1029/2001JC000955, 2002. 2418, 2422, 2436, 2466

Jenkins, A. D.: The use of a wave prediction model for driving a near-surface current model, Deut. Hydrogr. Z., 42, 133–149, 1989. 2421

Jordà, G., Bolaños, R., Espino, M., and Sánchez-Arcilla, A.: Assessment of the importance of the current-wave coupling in the shelf ocean forecasts, Ocean Sci., 3, 345–362, doi:10.5194/os-3-345-2007, 2007. 2420

Komar, P., Neudeck, R., and Kulm, L.: Shelf Sediment Transport, chap. Observations and significance of deep-water oscillatory ripple marks on the Oregon continental shelf, Hutchinson and Ross, Stroudsburg, Pa, 1972. 2419

Kumar, N., Voulgaris, G., and Warner, J.: Implementation and modification of a three-dimensional radiation stress formulation for surf zone and rip-current applications, Coast. Eng., 58, 1097–1117, 2011. 2420

Lazure, P. and Dumas, F.: An external-internal mode coupling for 3D hydrodynamical model for applications at regional scale (MARS), Adv. Water Resour., 31, 233–250, 2008. 2424

Lentz, S. J., Guza, R. T., Elgar, S., Feddersen, F., and Herbers, T. H. C.: Momentum balances on the North Carolina inner shelf, J. Geophys. Res., 104, 18205–18226, 1999. 2421

Lentz, S. J., Fewings, M., Howd, P., Fredericks, J., and Hathaway, K.: Observations and a Model of Undertow over the Inner Continental Shelf, J. Phys. Oceanogr., 38, 2341–2357, 2008. 2421

Leredde, Y. and Michaud, H.: Hydrodynamique sédimentaire sur le plateau continental du Golfe du Lion, in: Xèmes Journées Nationales Génie Cotier-Génie Civil, 14–16 octobre 2008, Sophia-Antipolis, 111–123, 2008. 2422

Longuet-Higgins, M.: On wave set-up in shoaling water with a rough sea bed., J. Fluid Mech., 527, 217–234, 2005. 2427

Longuet-Higgins, M. and Stewart, R.: Radiation stress and mass transport in gravity waves with application to surf beat, J. Fluid Mech., 13, 481–504, 1962. 2420

OSD

8, 2417–2478, 2011

Longuet-Higgins, M. S.: Mass Transport in Water Waves, Philos. T. R. Soc. Lond., 245, 535–581, 1953. 2427
Madec, G.: NEMO ocean engine, Note du Pole de modelisation, Institut Pierre-Simon Laplace (IPSL), France, no 27, 2008. 2443
Marsaleix, P., Auclair, F., and Estournel, C.: Considerations on open boundary conditions for regional and coastal ocean models, J. Atmos. Ocean. Tech., 23, 1604–1613, doi:10.1175/JTECH1930.1, 2006. 2427
Marsaleix, P., Auclair, F., Floor, J. W., Herrmann, M. J., Estournel, C., Pairaud, I., and Ulses, C.: Energy conservation issues in sigma-coordinate free-surface ocean models, Ocean Modell., 20, 61–89, doi:10.1016/j.ocemod.2007.07.005, 2008. 2418, 2421, 2422, 2424
Marsaleix, P., Auclair, F., and Estournel, C.: Low-order pressure gradient schemes in sigma coordinate models: The seamount test revisited, Ocean Modell., 30, 169–177, 2009a. 2418, 2422
Marsaleix, P., Ulses, C., Pairaud, I., Herrmann, M. J., Floor, J. W., Estournel, C., and Auclair, F.: Open boundary conditions for internal gravity wave modelling using polarization relations, Ocean Modell., 29, 27–42, 2009b. 2422
Mastenbroek, C., Burgers, G., and Janssen, P.: The dynamical coupling of a wave model and a storm surge model through the atmospheric boundary layer, J. Phys. Oceanogr, 23, 1856–1866, 1993. 2420
McWilliams, J. C., Restrepo, J. M., and Lane, E. M.: An asymptotic theory for the interaction of waves and currents in coastal waters, J. Fluid Mech., 511, 135–178, doi:10.1017/S0022112004009358, 2004. 2419, 2421, 2432
Mellor, G.: The Three-Dimensional current and surface wave equations, J. Phys. Oceanogr., 33, 1978–1989, 2003. 2419, 2432
Myrhaug, D., Holmedal, L. E., Simons, R. R., and MacIver, R. D.: Bottom friction in random waves plus current flow, Coast. Eng., 43, 75–92, 2001. 2430
Newberger, P. and Allen, J.: Forcing a three-dimensional, hydrostatic, primitive-equation model for application in the surf zone: 1. Formulation, J. Geophys. Res., 112, C08018, doi:10.1029/2006JC003472, 2007. 2419
Oltman-Shay, J., Howd, P., and Birkemeier, W.: Shear instabilities of the mean longshore current: Field Observation, J. Geophys. Res., 94, 18031–18042, 1989. 2445
Ozkan-Haller, T. and Kirby, J.: Nonlinear evolution of shear instabilities of the longshore current: a comparison of observation and computations, J. Geophys. Res., 104, 25953–25984, 1999.

OSD
8, 2417–2478, 2011

2445
Palanques, A., Puig, P., Guillén, J., Durrieu de Madron, X., Latasa, M., Scharek, R., and Martin, J.: Effects of storm events on the shelf-to-basin sediment transport in the southwestern end of the Gulf of Lions (Northwestern Mediterranean), Nat. Hazards Earth Syst. Sci., 11, 843–850, doi:10.5194/nhess-11-843-2011, 2011. 2448
Phillips, O.: The dynamics of the upper ocean, Cambridge University Press, London, 336 pp., 1977. 2420
Rascle, N.: Impact des vagues sur la circulation océanique, Ph.D. thesis, Université de Bretagne Occidentale, 2007. 2419
Rascle, N. and Ardhuin, F.: Drift and mixing under the ocean surface revisited: Stratified conditions and model-data comparisons, J. Geophys. Res., 114, C02016, doi:10.1029/2007JC004466, 2009. 2420
Rascle, N., Ardhuin, F., and Terray, E. A.: Drift and mixing under the ocean surface: A coherent one-dimensional description with application to unstratified conditions, J. Geophys. Res., 111, C03016, doi:10.1029/2005JC003004, 2006. 2426, 2429, 2435
Rascle, N., Ardhuin, F., Queffeulou, P., and Croizé-Fillon, D.: A global wave parameter database for geophysical applications. Part I: Ave-current-turbulence interaction parameters for the open ocean based on traditional parameterizations, Ocean Modell., 25, 154–171, 2008. 2429
Reniers, A., Symonds, G., and Thornton, E.: Modelling of rip currents during rdex, in: Coastal Dynamics '01: Proceedings, edited by: Hanson, H. and Larson, M., 493–499, Amer. Soc. Civil Engineers, Coasts, Oceans, Ports & Rivers Inst, 4th International Conference on Coastal Dynamics, Lund, Sweden, 11–15 June 2001, 2001. 2444
Reniers, A., Roelvink, J., and Thornton, E.: Morphodynamic modeling of an embayed beach under wave group forcing, J. Geophys. Res., 109, C01030, doi:10.1029/2002JC001586, 2004. 2419
Rusu, E. and Soares, C. G.: Numerical modelling to estimate the spatial distribution of the wave energy in the Portuguese nearshore, Renew. Energ., 34, 1501–1516, 2009. 2431
Serrat, P., Ludwig, W., Navarro, B., and Blazi, J.: Variabilité spatio-temporelle des flux de maières en suspension d'un fleuve côtier méditerranéen: la Têt (France), Comptes Rendus de l'Académie des Sciences, D333, 389–397, 2001. 2439
Shchepetkin, A. and McWilliams, J.: The regional oceanic modeling system (ROMS): a split-explicit, free-surface, topography-following-coordinate oceanic model, Ocean Modell., 9,

OSD
8, 2417–2478, 2011

347–404, doi:10.1016/j.ocemod.2004.08.002, 2005. 2424, 2432
Smith, R.: Reflection of short gravity waves on a non-uniform current, Math. Proc. Cambridge Philos. Soc., 78, 517 pp., 1975. 2420
Soulsby, R., Stive, M., de Vriend, H., Fredsoe, J., Hamm, L., Teisson, C., and Winterwerp, J.: Bed shear stresses due to combined waves and current, Advances in coastal morphodynamics, 4, 20–23, 1995. 2429
Stokes, G.: On the theory of oscillatory waves, Transactions of the Cambridge Philosophical Society, 8, 441–455, 1847. 2419
Svendsen, I. A., Haas, K., and Zhao, Q.: Shorecirc -the quasi-3d nearshore circulation model, Tech. Rep. Technical report CACR-02-01, University of Delaware, Center for Applied Coastal Research, 2002. 2432
Taylor, G.: Standing waves on a contracting or expanding current, J. Fluid Mech., 13, 182–194, 1962. 2420
Terray, E. A., Donelan, M., Agrawal, Y., Drennan, W., Kahma, K., Williams, A., Hwang, P., and Kitaigorodskii, S.: Estimates of kinetic energy dissipation under breaking waves, J. Phys. Oceanogr., 26, 792–807, 1996. 2428, 2429
Terray, E. A., Drennan, W., and Donelan, M.: The vertical structure of shear and dissipation in the ocean surface layer, Proc. Symp. on Air-Sea Interaction, 239–245, 2000. 2429
Tolman, H.: A mosaic approach to wind wave modeling, Ocean Modell., 25, 35–47, doi:10.1016/j.ocemod.2008.06.005, 2008. 2418, 2425
Tolman, H.: User Manual and system documentation of WAVEWATCH-III version 3.14. Technical Report, Tech. Rep. 276, NOAA/NWS/NCEP/MMAB, 2009. 2418, 2425
Tonani, M., Pinardi, N., Dobricic, S., Pujol, I., and Fratianni, C.: A high-resolution free-surface model of the Mediterranean Sea, Ocean Sci., 4, 1–14, doi:10.5194/os-4-1-2008, 2008. 2443
Trampenau, T., Oumeraci, H., and Dette, H.: Hydraulic functioning of permeable pile groins, J. Coastal Res., 33, 160–187, 2004. 2445
Uchiyama, Y., McWilliams, J. C., and Shchepetkin, A. F.: Wave-current interaction in an oceanic circulation model with a vortex-force formalism: Application to the surf zone, Ocean Modell., 34, 16–35, doi:10.1016/j.ocemod.2010.04.002, 2010. 2418, 2419, 2421, 2422, 2426, 2432
Ulses, C.: Dynamique océanique et transport de la matière particulaire dans le Golfe du Lion: Crue, tempête et période hivernale, Ph.D. thesis, Université Paul Sabatier Toulouse, 2005. 2422
Ulses, C., Estournel, C., Bonnin, J., Durrieu de Madron, X., and Marsaleix, P.: Impact of storms

OSD
8, 2417–2478, 2011

and dense water cascading on shelf-slope exchanges in the Gulf of Lion (NW Mediterranean), J. Geophys. Res., 113, C02010, doi:10.1029/2006JC003795, 2008a. 2438
Ulses, C., Estournel, C., Durrieu de Madron, X., and Palanques, A.: Suspended sediment transport in the Gulf of Lions (NW Mediterranean): Impact of extreme storms and floods, Cont. Shelf Res., 28, 2048–2070, doi:10.1016/j.csr.2008.01.015, 2008b. 2444, 2448
Ulses, C., Estournel, C., Puig, P., Durrieu de Madron, X. D., and Marsaleix, P.: Dense shelf water cascading in the northwestern Mediterranean during the cold winter 2005: Quantification of the export through the Gulf of Lion and the Catalan margin, Geophys. Res. Lett., 35, L07610, doi:10.1029/2008GL033257, 2008c. 2422
Weaver, P., Canals, M., and Trincardi, F.: EUROSTRATAFORM Special Issue of Marine Geology, Mar. Geol., 234, 1–2, doi:10.1016/j.margeo.2006.09.001, 2006. 2439
Weir, B., Uchiyama, Y., Lane, E. M., Restrepo, J. M., and Williams, J. M.: A vortex force analysis of the interaction of rip currents and surface gravity waves, J. Geophys. Res., 116, C05001, doi:10.1029/2010JC006232, 2011. 2421, 2437
Whitham, G.: Mass, momentum and energy flux in water waves, J. Fluid Mech., 12, 135–147, 1962. 2420
Xu, Z. and Bowen, A.: Wave- and wind-driven flow in water of finite depth, J. Phys. Oceanogr., 24, 1850–1866, 1994. 2420

OSD
8, 2417–2478, 2011

Table 1. Computational grids used in this study: $N\lambda$ and $N\theta$ are the numbers of points in longitude λ and latitude θ, and δt is the maximum global time step.

Grids	Resolution	Latitude	Longitude	$N\lambda$	$N\theta$	δt (s)
WW3-MEDOC	0.1°	31 to 45° N	−5.6 to 16.3° E	141	220	400
WW3-GoL	0.02°	41.28 to 44.45° N	2.02 to 11.86° E	117	213	300
Grids	Maximum Resolution	Minimum Resolution	Latitude	Longitude	Number of nodes	δt (s)
WW3-TET	22 m	550 m	42.272 to 43.158° N	3.018 to 3.621° E	64 000	5

OSD
8, 2417–2478, 2011

Table 2. Statistical comparison between data and simulations at WW3-TET scale, at SODAT and POEM.

Position	Parameters	COR	BIAS	RMSE	SI
SODAT (11 m)	Period	0.5833	−0.2574 s	2.3137	0.4133
	Wave height	0.9580	0.1841 m	0.2869	0.2727
POEM (28 m)	Period	0.7203	−0.1279 s	1.4206	0.3103
	Wave height	0.9330	0.2311 m	0.3507	0.3345

OSD
8, 2417–2478, 2011

Table 3. Computational grids used in the circulation model. i_{max} and j_{max} are respectively the numbers of points in the west-east and south-north directions.

Grids	Resolution	Longitude	Latitude	i_{max}	j_{max}	levels
MEDOC	2500 m	−0.39 to 11.65° E	38.39 to 44.44° N	402	270	40
GoL	800 m	3.03 to 5.75° E	41.98 to 43.57° N	278	222	36
TET	from 8 to 180 m	3.027 to 3.313° E	42.506 to 42.925° N	378	394	15

OSD
8, 2417–2478, 2011

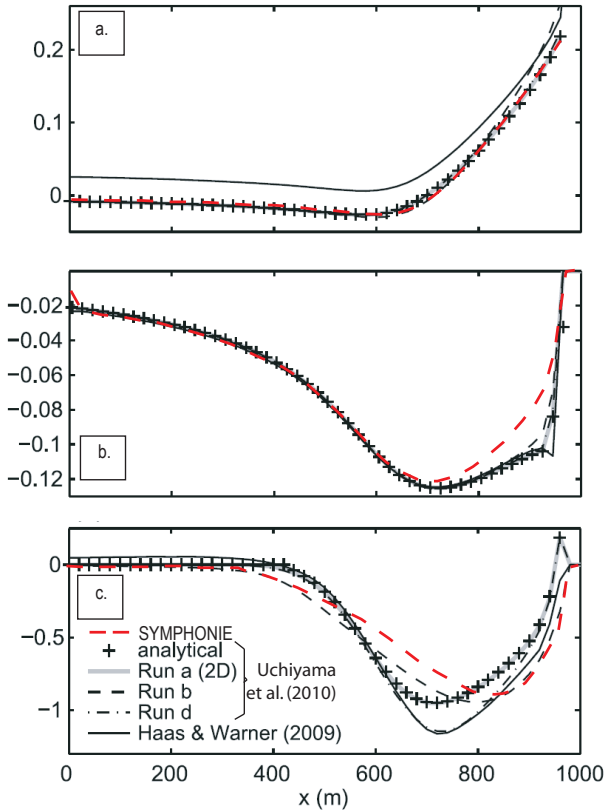

Fig. 1. Cross-shore profile of the surface elevation **(a)**, barotropic quasi-Eulerian cross-shore **(b)** and longshore **(c)** velocities ($m\,s^{-1}$) (adapted from UMS10). SYMPHONIE results are the red dashed line whereas ROMS results of run b are in black dashed line. The shoreline is at right.

OSD
8, 2417–2478, 2011

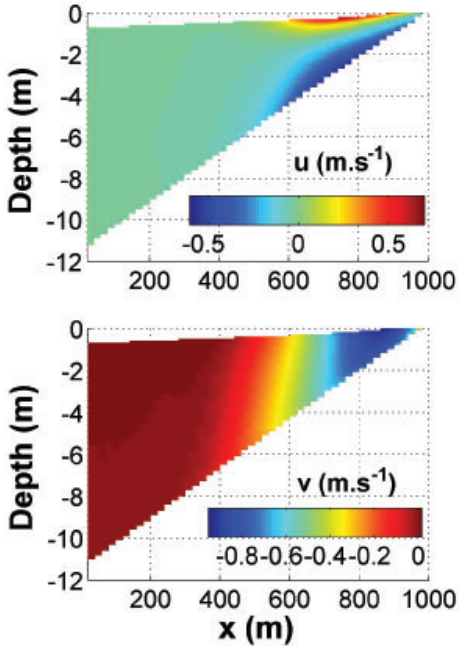

Fig. 2. Vertical sections of quasi-Eulerian cross-shore (top) and longshore (bottom) velocities in SYMPHONIE.

OSD
8, 2417–2478, 2011

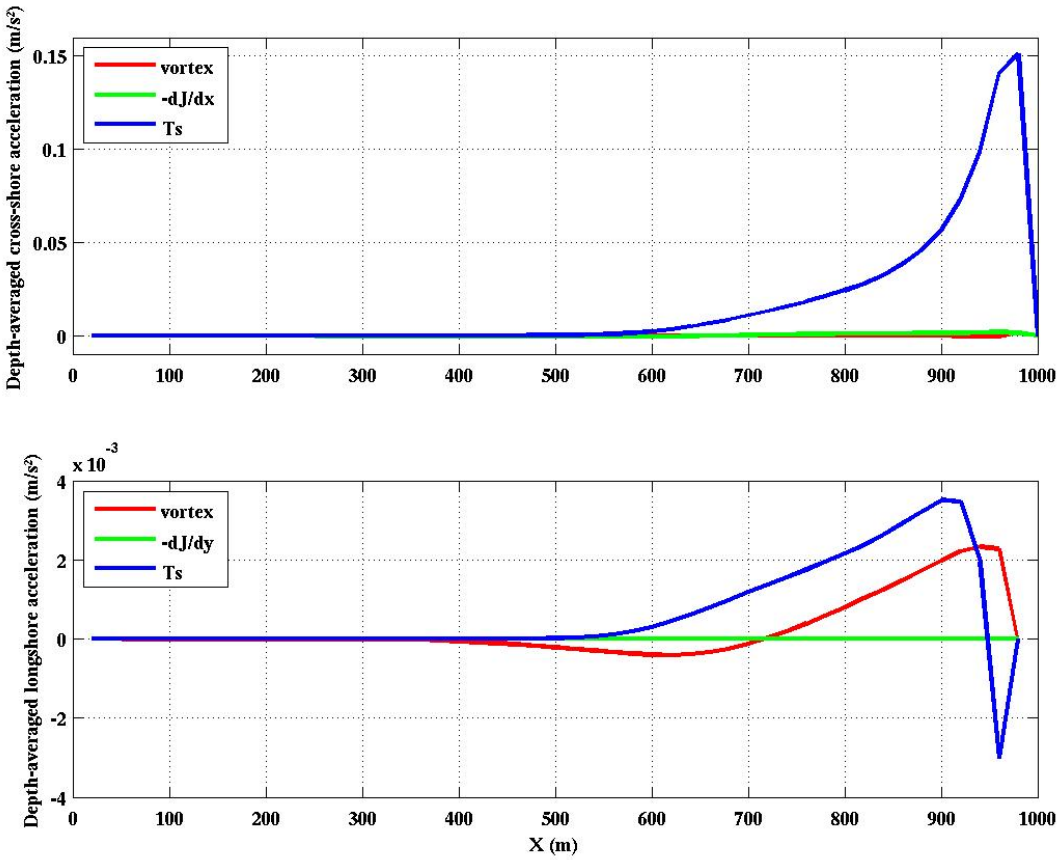

Fig. 3. Depth-averaged values of the different wave-induced forcing terms of the mean flow in the cross-shore (top) and longshore (bottom) momentum balance, versus cross-shore distance: the surface momentum flux T_s (blue), the vortex force (red) and the Bernouilli pressure head $-\nabla J$ (green).

OSD
8, 2417–2478, 2011

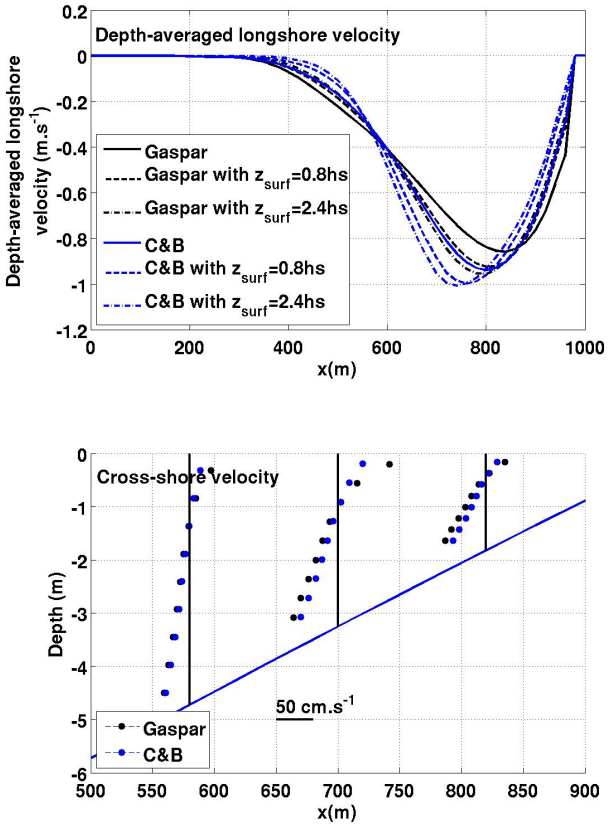

Fig. 4. Top: cross-shore profile of the longshore depth-averaged velocities for different surface boundary conditions Gaspar et al. (1990) or Craig and Banner (1994) and different mixing length in the turbulence closure. Bottom: comparison of vertical profiles of the cross-shore velocities by using the parameterization of Gaspar et al. (1990) or Craig and Banner (1994).

OSD
8, 2417–2478, 2011

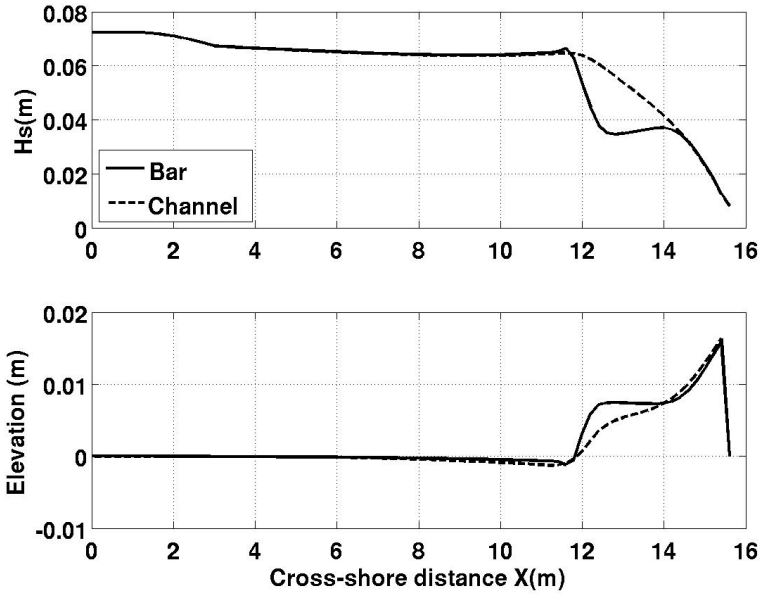

Fig. 5. Significant wave height (top) and surface elevation (bottom) versus cross-shore distance over the center bar at $y = 9.2$ m (solid line) and through the rip channel at $y = 4.6$ m (dashed line). The shoreline is at right.

OSD
8, 2417–2478, 2011

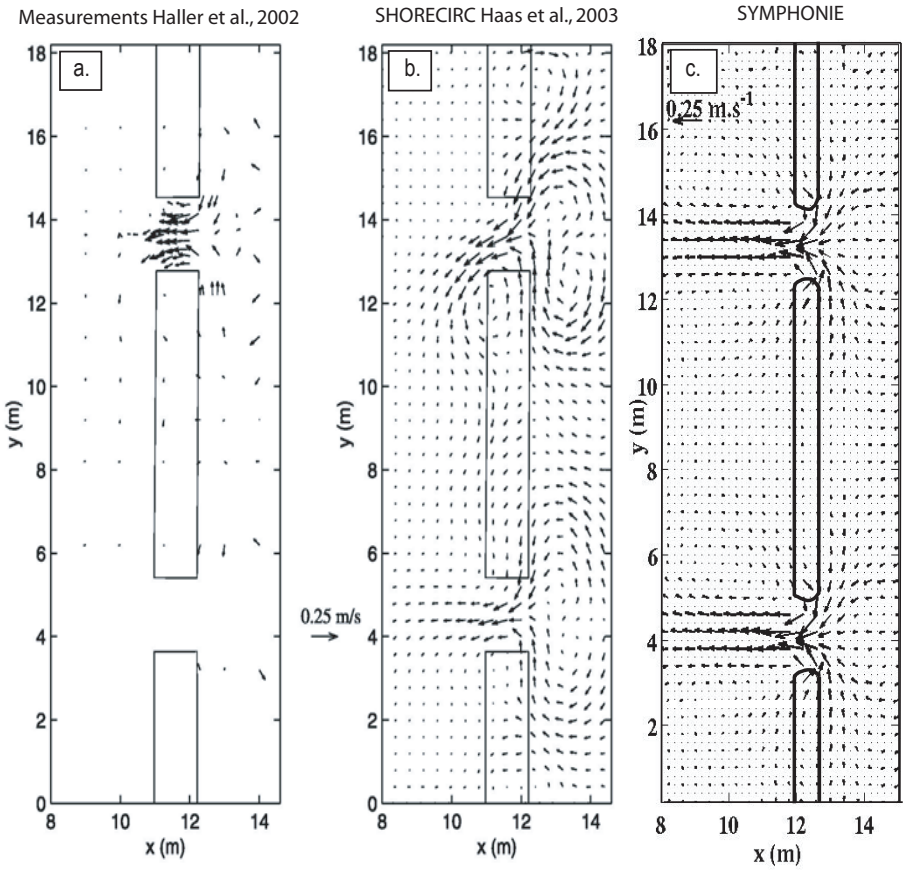

Fig. 6. Comparison of depth-integrated current measured by Haller et al. (2002) **(a)**, with numerical simulations done by SHORECIRC (Haas et al., 2003) **(b)** and SYMPHONIE **(c)**.

OSD
8, 2417–2478, 2011

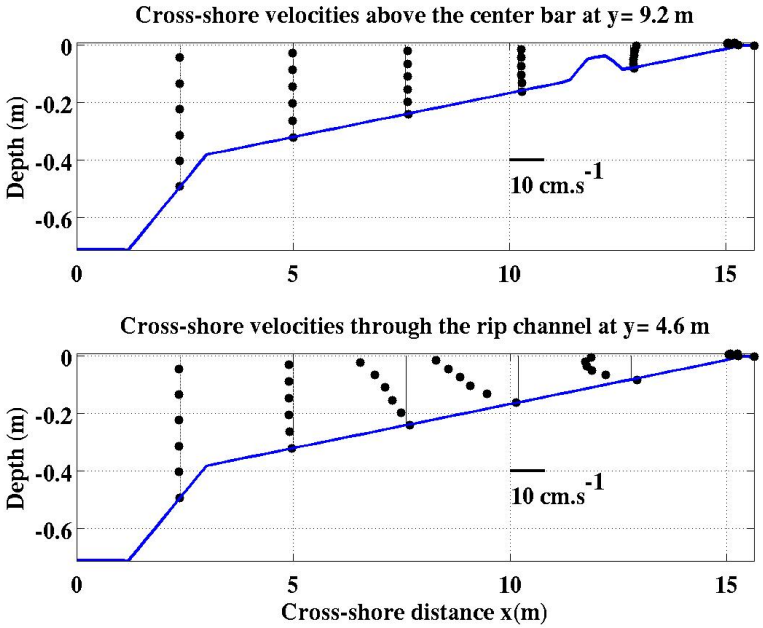

Fig. 7. Vertical profiles of the cross-shore velocities versus cross-shore distance, above the center bar (upper panel) and through a rip channel (lower panel).

OSD
8, 2417–2478, 2011

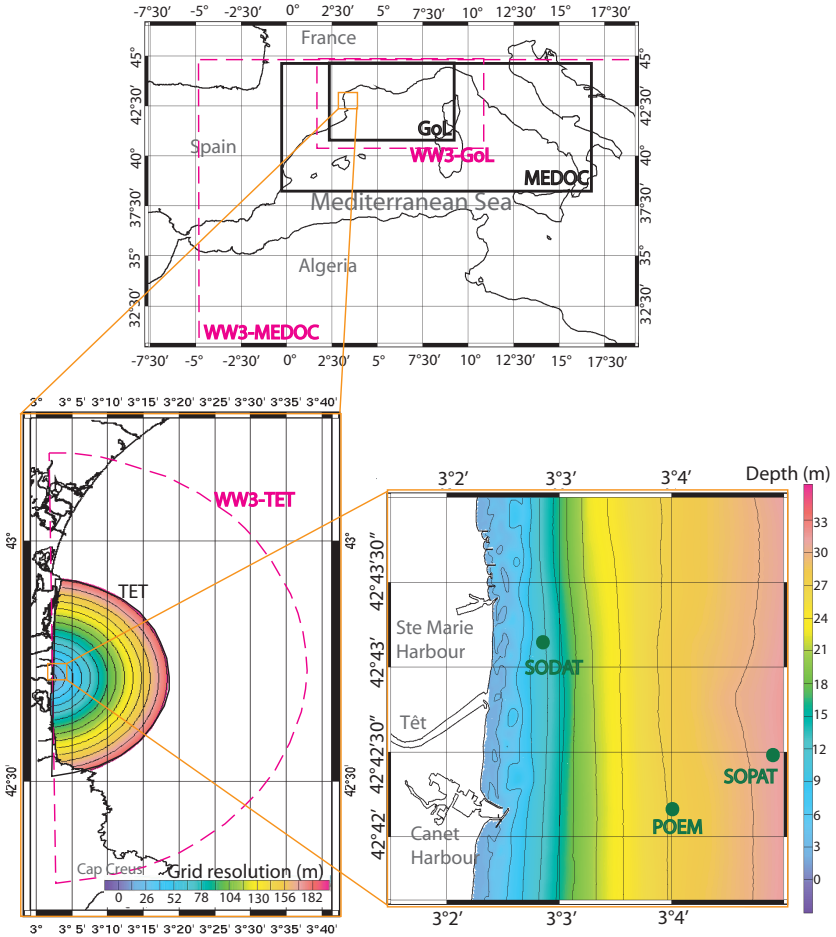

Fig. 8. The three embedded domains used by SYMPHONIE (black frame) and WW3 (dashed pink frame) for the Têt inner shelf simulation and positions of the three instruments.

OSD
8, 2417–2478, 2011

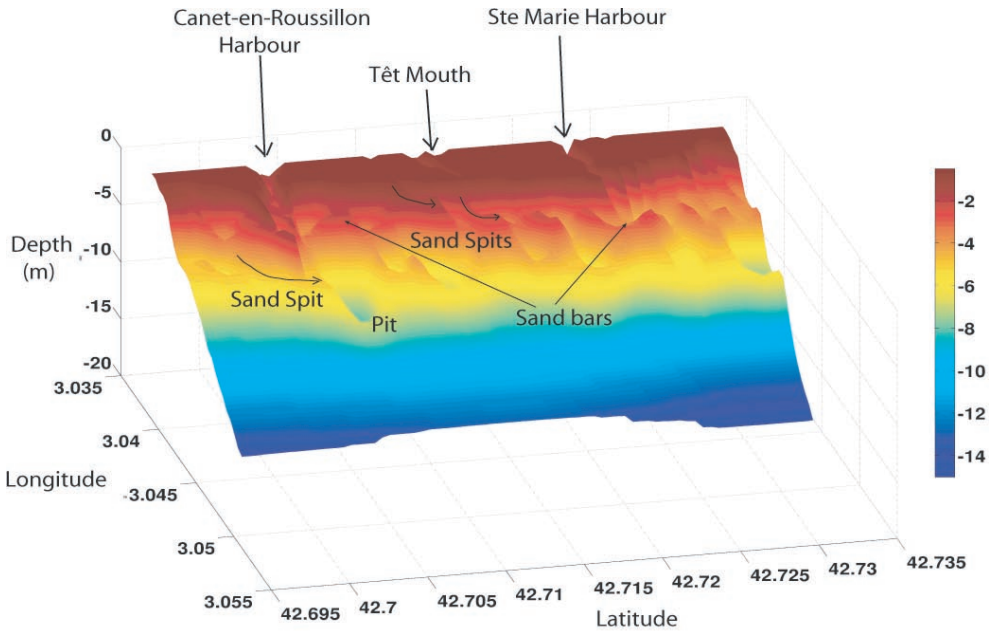

Fig. 9. The Têt bathymetry measured by the LiDAR survey. The developments of northward sand spits in front of the river mouth or the Canet-en-Rousillon harbour are clearly visible.

OSD
8, 2417–2478, 2011

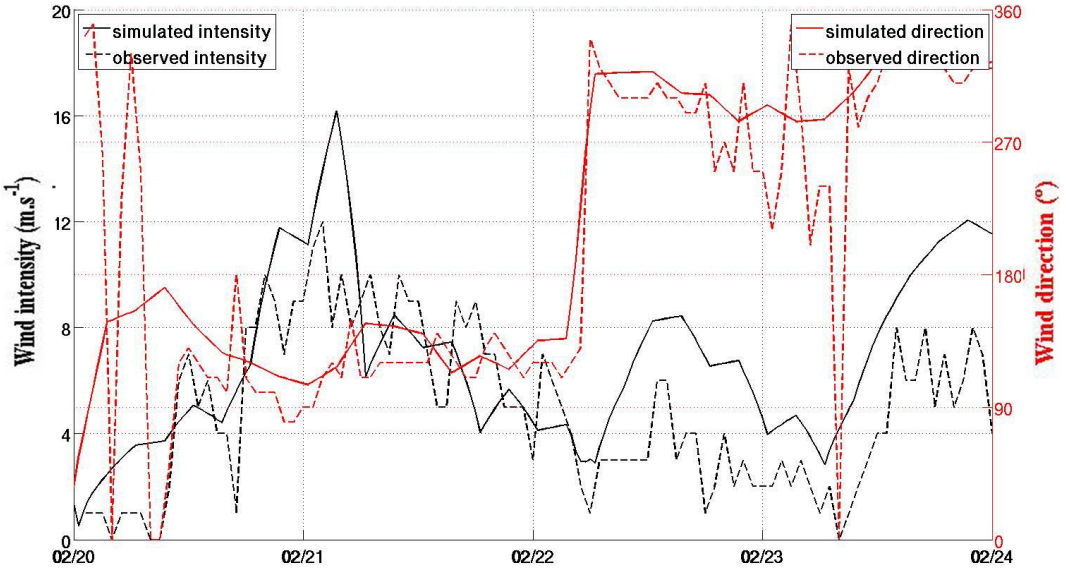

Fig. 10. Simulated (solid line) and observed (dashed line) wind intensity (black) and direction (red). The data are provided by the Toreilles station and simulated wind is given at the SODAT station.

OSD
8, 2417–2478, 2011

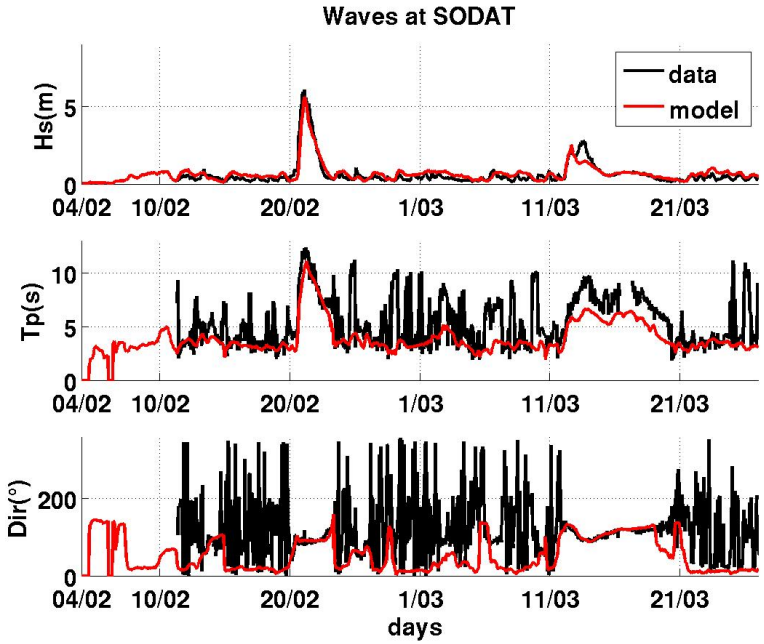

Fig. 11. Comparison of wave parameters between data and simulation at SODAT (11 m).

OSD
8, 2417–2478, 2011

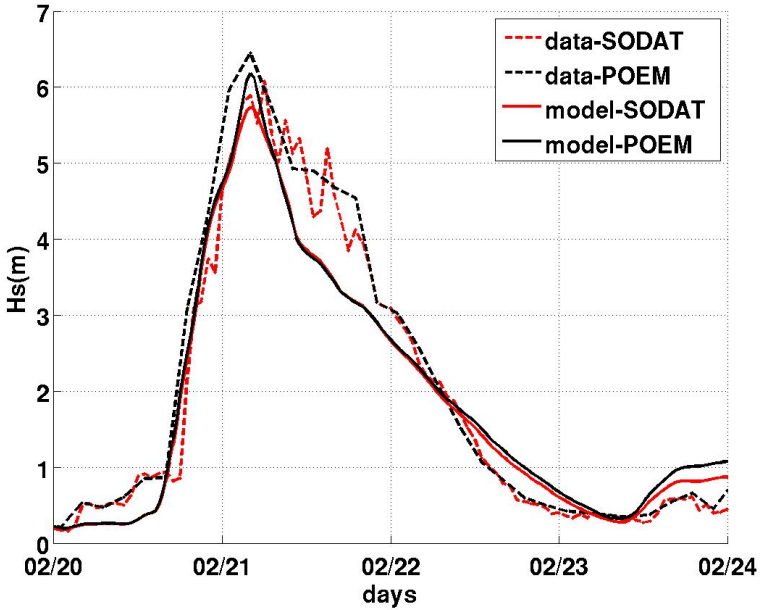

Fig. 12. Comparison of significant wave height at SODAT (11 m) and POEM (28 m) in the model and the measurements.

OSD
8, 2417–2478, 2011

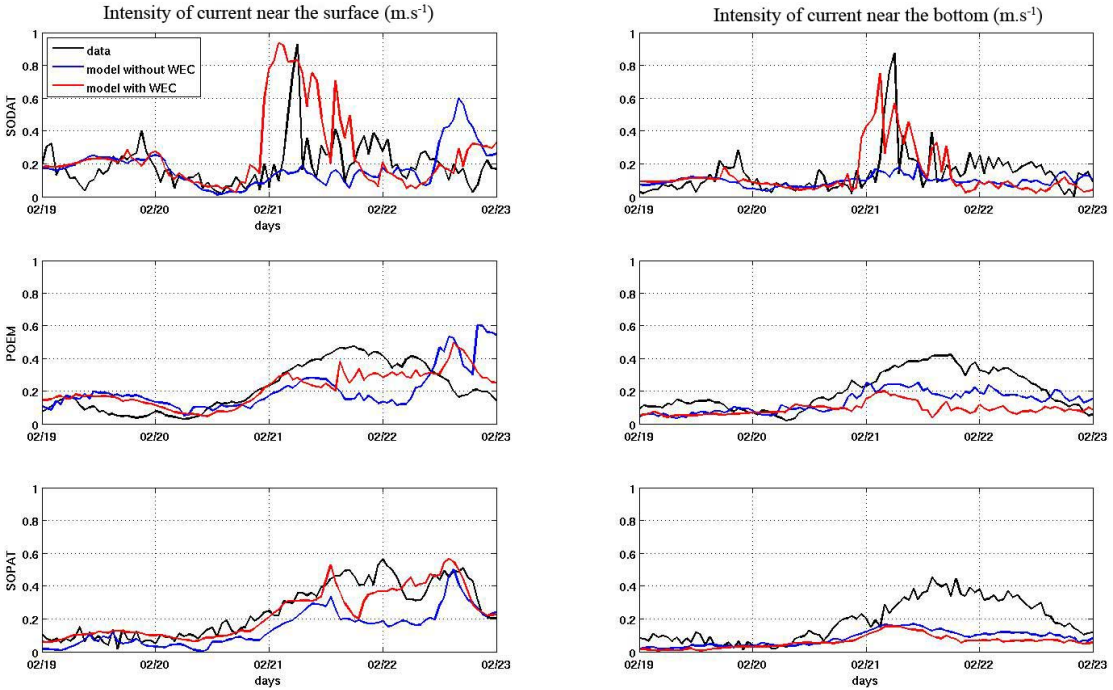

Fig. 13. Comparison of the current intensity near the bottom (right) and close to the surface (left) at the three instruments, between the measured current (black) and the simulated current with (with WEC – red) and without the wave forcing (without WEC – blue).

OSD
8, 2417–2478, 2011

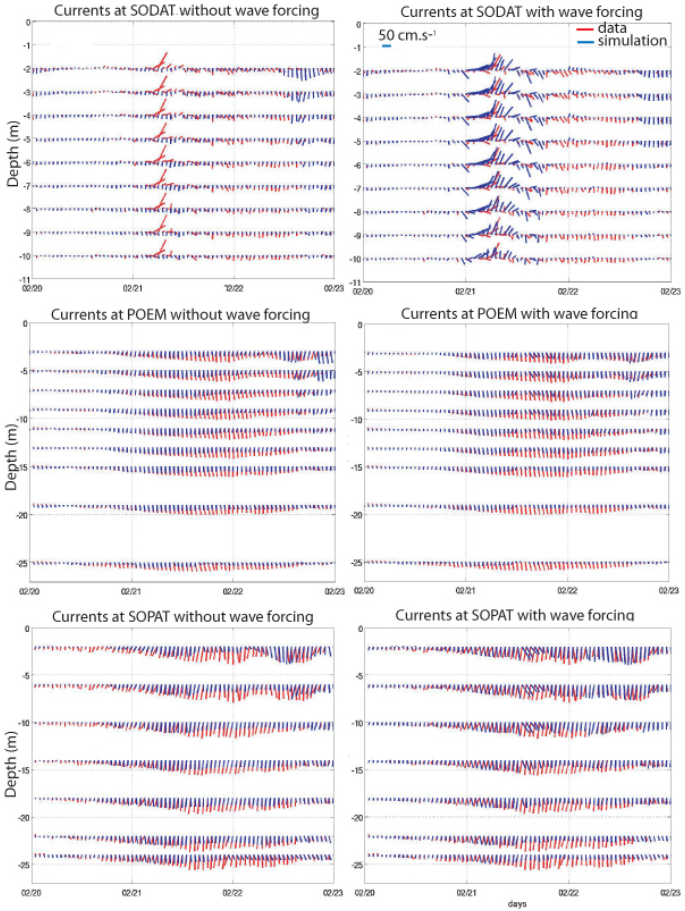

Fig. 14. Comparison of time series at the three instruments, between the measured current and the simulated current. Left: the simulation is performed without the wave forcing, and right: the simulation is performed with the wave forcing.

OSD
8, 2417–2478, 2011

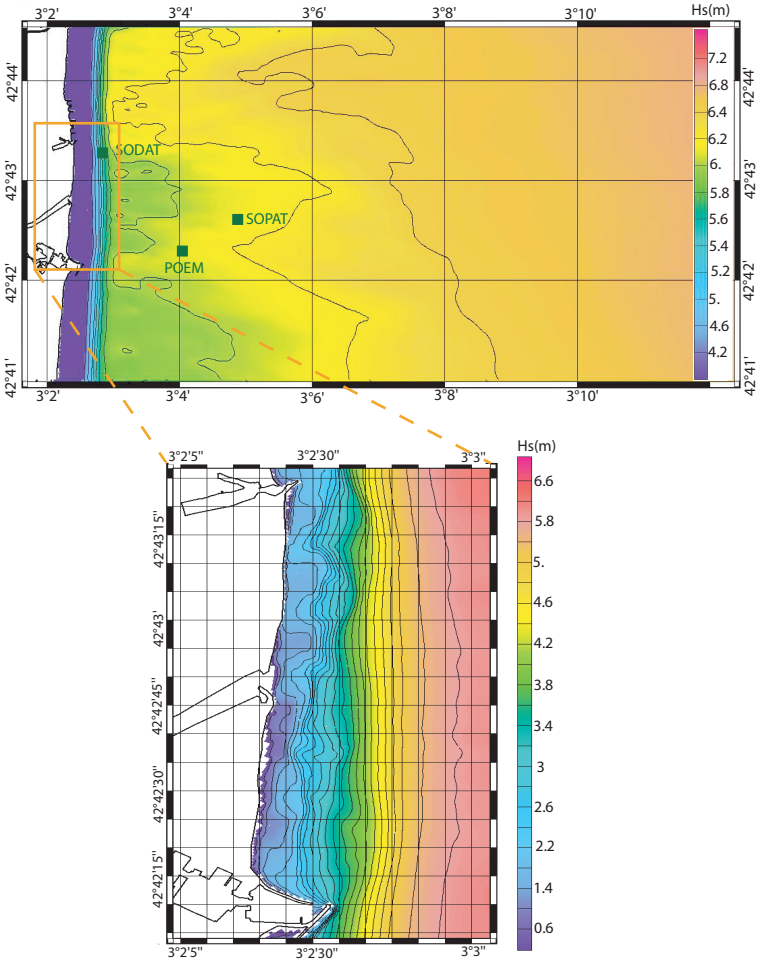

Fig. 15. Significant wave height at the storm apex on 21 February 2004 at 04:19 a.m.

OSD
8, 2417–2478, 2011

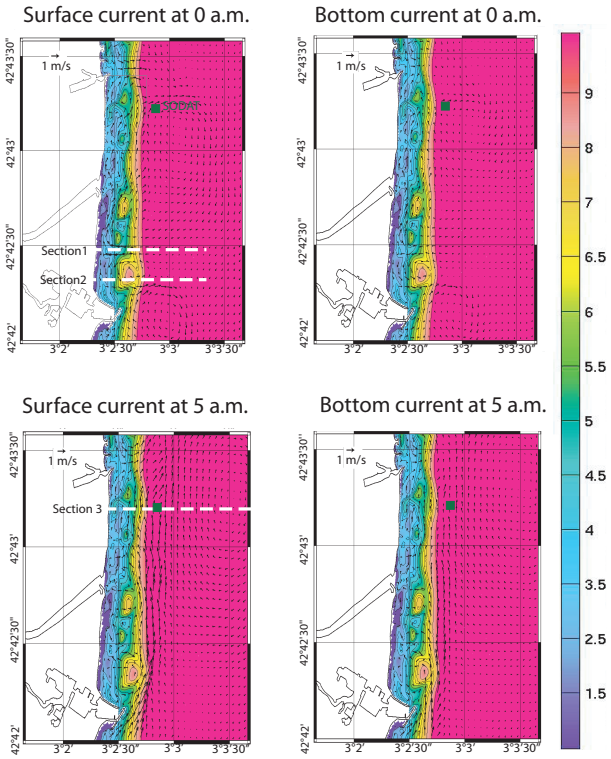

Fig. 16. Two different current patterns at an interval of 5 h:

- Surface and bottom current on 21 February at 00:00 a.m. during the intensified stage of the storm
- Surface and bottom current on 21 February at 05:00 a.m. at the storm apex

The color palette indicates the bathymetry whereas the arrows are the current vector. Position of the SODAT instrument is indicated with the green spot, as well as the position of the cross-shore sections of the following figure.

OSD
8, 2417–2478, 2011

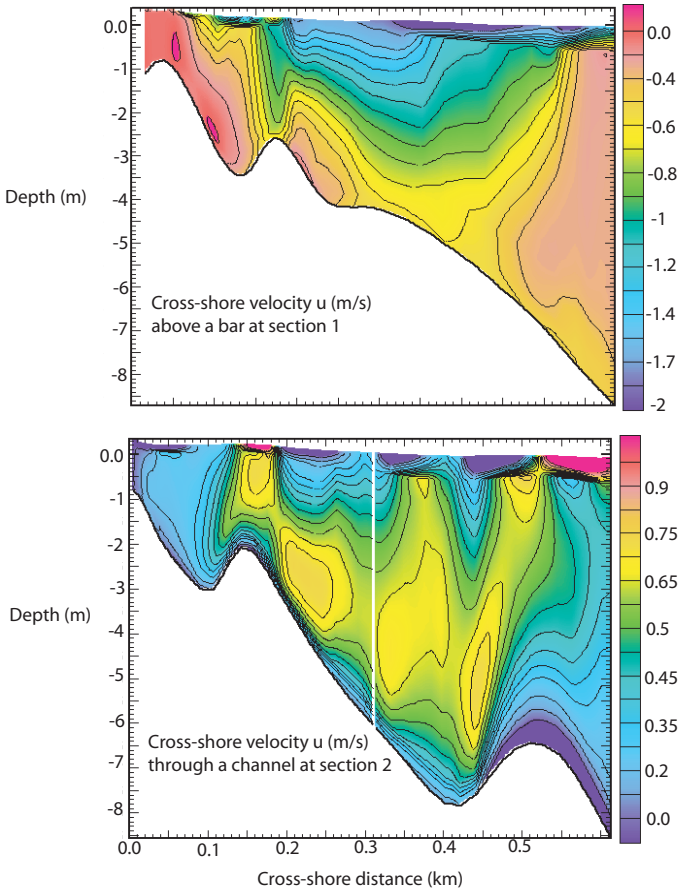

Fig. 17. Vertical sections of the cross-shore velocity above a bar (top, Sect. 1) and through a channel (bottom, Sect. 2) during the intensified stage of the storm. Positions of the sections are indicated in Fig. 16.

OSD
8, 2417–2478, 2011

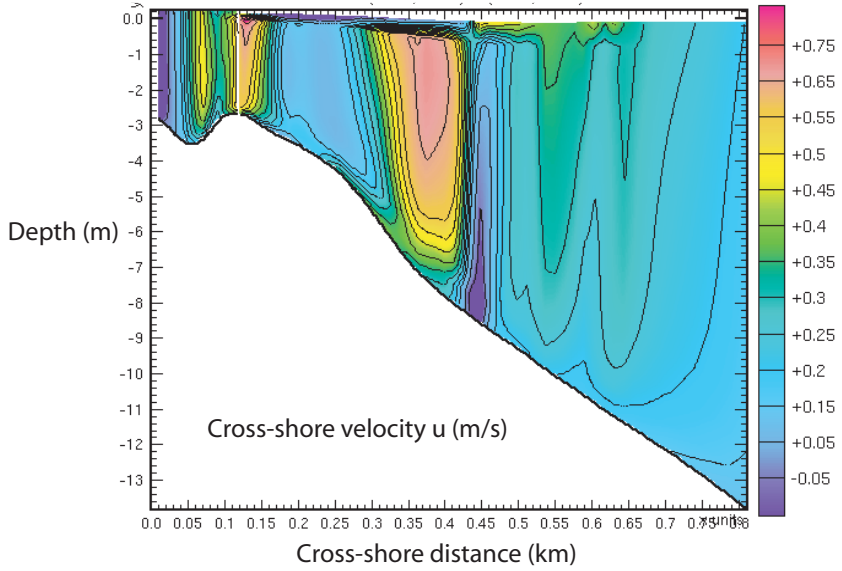

Fig. 18. Vertical section (corresponding to Sect. 3 in Fig. 16) of the cross-shore velocity at the storm apex.

OSD
8, 2417–2478, 2011